Engineering Geology 361 (2026) 108495

Contents lists available at ScienceDirect

Engineering Geology

journal homepage: www.elsevier.com/locate/enggeo

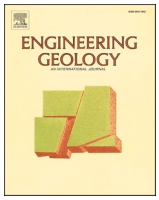

A 3D multiphase SPH framework for modelling soil-water interaction in rainfall-landslide-tsunami cascades

Ruofeng Feng *, Jidong Zhao *, Jianyu Chen

Department of Civil and Environmental Engineering, Hong Kong University of Science and Technology, China

ARTICLE INFO

Keywords:
Smoothed particle hydrodynamics
Large deformation
Hydro-mechanical coupling
Multi-hazard cascades
Geophysical flows

ABSTRACT

Multi-hazard cascades, in which multiple hazards interact through one or more natural processes, are an increasing concern worldwide. Among them, landslide-tsunami events represent one of the most significant cascading hazards due to their destructive potential. Computational modelling of the entire cascading process, from the initial triggering to the amplification of risks as the events evolve, is critical, and has attracted growing interest within the research community. This paper presents a novel three-dimensional multiphase smoothed particle hydrodynamics (SPH) model to address this challenge. The proposed framework provides a unified approach for simulating coupled soil-water interactions, including pore water flow in saturated and unsaturated soils, soil deformation, and the dynamic interaction between landslide masses and external water bodies. Key innovations and contributions of the model include: (1) the introduction of a numerical density concept to mitigate issues arising from discontinuities in physical density at interphase interfaces; (2) the integration of *u–w–p* formulation of Biot's theory into the multiphase model to accurately capture coupled flow–deformation behaviour in saturated and unsaturated soils; (3) an extension of the δ-SPH scheme to ensure a smooth and stable pressure field for both external water and internal pore water; (4) robust treatment for solid and hydraulic boundaries specific to coupled soil-water problems; (5) implementation within a CUDA-based, GPU-accelerated framework for large-scale 3D applications. The model is rigorously validated against a series of benchmark tests and finally applied to the 3D simulation of a rainfall–landslide–tsunami cascade. The results demonstrate that the proposed framework effectively captures the entire hazard cascading process, from rainfall infiltration, landslide initiation and motion, and tsunami generation and propagation, to the final impacts such as overtopping and flooding. This represents a significant advance in computational modelling of geophysical multi-hazard cascades.

1. Introduction

Coupled soil-water interaction is a fundamental process governing a wide range of geophysical phenomena, such as wave-induced seabed liquefaction, sediment scouring, and submarine landslides. It is also a primary driver responsible for the occurrence of cascading hazards such as rainfall-landslide-tsunami sequence.

The response of soil to water infiltration, particularly during rainfall events, is a transient hydrological process governed by factors such as soil moisture, flow intensity, and the resulting pore water pressure (Iverson, 2000). Heavy rainfall can increase pore water pressure, which in turn reduces the effective stress within the soil and weakens the stability of slopes and geotechnical structures. This mechanism has triggered numerous catastrophic cascade events. For example, in 2007, the combination of intense rainfall and changes in reservoir water levels triggered a landslide at China's Shuibuya Reservoir, resulting in a 50-m-high impulse wave on the far side of the reservoir (Wang et al., 2021). Likewise, changes in reservoir levels and precipitation were critical factors in the Vajont disaster in Italy, where a significant landslide produced a large wave that overtopped the dam, leading to more than 2000 fatalities (Paronuzzi and Bolla, 2012). In another case, substantial rainfall caused a landslide and subsequent tsunami in Vietnam's Tra Giang River, which generated a wave with a peak height of 8.5 m and caused one fatality (Duc et al., 2020). More recently, heavy rainfall from an extratropical cyclone triggered a landslide-tsunami cascade in Todos los Santos Lake, Chile, impacting the town of Petrohué within one minute of slope failure (Aránguiz et al., 2023).

The devastating potential of these cascading hazards makes the accurate prediction and understanding of their underlying mechanisms a critical scientific imperative. However, integrated computational

* Corresponding authors.
E-mail addresses: ruofengfeng@ust.hk (R. Feng), jzhao@ust.hk (J. Zhao).

https://doi.org/10.1016/j.enggeo.2025.108495
Received 2 October 2025; Received in revised form 11 November 2025; Accepted 3 December 2025
Available online 4 December 2025

modelling of these events remains profoundly challenging: violent free-surface water flow, hydro–mechanical coupling, massive soil movement, and the interaction of sliding masses with water, all combine nonlinearly on a large scale. A significant step toward addressing these challenges is the development of the sequential analysis tools LS-RAPID and LS-Tsunami by Sassa et al. (2016), which have been adopted by the International Consortium on Landslides (ICL). As demonstrated in the study of the Tra Giang event by Duc et al. (2020), these tools simulate the landslide and tsunami in separate, sequential steps. LS-RAPID is used to simulate landslide initiation and motion, with an empirically chosen increase in pore water pressure ratio to model the rainfall trigger. The computed landslide dynamics are then transferred to the LS-Tsunami model for modelling the generation and propagation of the resulting tsunami. This two-step sequential coupling process, while efficient, fails to capture the essential multi-physical evolution as well as the dynamic interaction between soil and water during the hazard cascade and thus the analysis may often involve empiricism and uncertainties. This limitation underscores the need for a single, unified numerical framework capable of continuously modelling the entire hazard chain from triggering to final impact. The development of such a framework is essential for advancing physics-based risk management strategies, such as the creation of predictive digital twins (Torzoni et al., 2024; Ju et al., 2025) and rigorous process-based risk assessment (Vega and Hidalgo, 2016). Beyond physical fidelity, a unified approach also offers computational advantages, such as consistent interface treatment, solution adaptivity, and streamlined parallel scalability.

Continuum-based meshfree methods have emerged as powerful tools to bridge this gap, owing to their inherent ability to handle extreme deformations and complex multi-physics interactions. Prominent examples include the material point method (MPM) (Yerro et al., 2019; Yu et al., 2024, 2025; Cheng et al., 2026), peridynamics (PD) (Yang et al., 2024, 2025), and smoothed particle hydrodynamics (SPH) (Chen et al., 2020, 2021; Bui and Nguyen, 2021; Feng et al., 2025a). Among these, SPH is a truly meshfree, Lagrangian particle method that has demonstrated unparalleled capability in simulating highly nonlinear free-surface flows (Sun et al., 2017; Zhang et al., 2017; Khayyer et al., 2018) and fluid-structure interactions (Dai et al., 2017, 2023a). Its application has recently expanded to geomechanics, proving effective for problems involving large soil deformations (e.g., Feng et al., 2021; Zhang et al., 2024a, 2024b; Zhang et al., 2025; Lian et al., 2024; Ma et al., 2024; Su et al., 2026). The multiphase SPH method, which solves multiple phases within a unified framework, is capable of accurately and consistently capturing dynamic interactions across multiple continua and complex interfacial topological changes, making it a promising tool for addressing the previously mentioned challenges. The multiphase SPH method is conventionally applied to multi-fluid systems, such as air–water interaction (Hammani et al., 2020; Ren et al., 2024), multi-fluid mixing (Meng et al., 2020), and water–sediment interaction (Zubeldia et al., 2018). More recently, it has been extended through the incorporation of soil constitutive models to study soil–water interactions for applications such as dam surface erosion (Zhou et al., 2024), submarine landslides (Kamani et al., 2025; Yi et al., 2025), bridge scouring (Zhang et al., 2024a, 2024b), and landslide-tsunami cascades (Dai et al., 2023b, 2025). However, a major limitation of most existing multiphase models is their treatment of soil using a total stress approach under undrained conditions, which precludes the simulation of critical hydraulic processes like rainfall infiltration and pore pressure dissipation. While recent advances in hydro-mechanically coupled SPH models have demonstrated success in modelling coupled flow–deformation processes in unsaturated and saturated soils, particularly for rainfall-induced landslides (e.g., Feng et al., 2022, 2024a; Lian et al., 2024; Nguyen et al., 2025), a unified framework that integrates all processes from the triggering and onset of soil instability to post-failure flow and cascading events has not yet been established.

To address this critical gap, this work develops a novel 3D multiphase SPH model for the unified description of the pore water flow in saturated/unsaturated soils, coupled pore flow-soil deformation, and the interaction of soil with external water. The concept of numerical density is introduced for the consistent description of density evolution and mitigating issues associated with discontinuities in physical density at interphase interface. The *u-w-p* formulation of Biot's theory for unsaturated/saturated porous material is incorporated into the multiphase framework to capture coupled flow–deformation behaviour in soils. In addition, the widely used δ-SPH model for free-surface flows is extended to enable unified modelling of the external water and pore water in soils with a smooth pressure field. Furthermore, solid boundary treatments for both soil and water phases, as well as hydraulic boundary treatments for pore water flow, are investigated. The proposed model is rigorously validated through a series of benchmarks, including 1D infiltration/evaporation, the Liakopoulos drainage test, the Fei Tsui Road rainfall-induced landslide, and a laboratory-scale landslide-generated tsunami experiment. Finally, its capability is demonstrated by conducting a full 3D simulation of a cascading rainfall-landslide-tsunami event.

The remainder of this paper is organised as follow: Section 2 presents the mathematical formulation of the unified multiphase soil-water model. The multiphase SPH discretization and numerical implementation are detailed in Section 3. Validation cases are presented in Section 4, and the application to 3D cascading events is shown in Section 5. Concluding remarks are summarized in Section 6.

2. Mathematical model for the soil-water system

2.1. Mass and momentum balance equation

The Lagrangian formulation of mass and momentum balance equations in continuum mechanics for the unified description of the multiphase system is written as,

$$\frac{d^{\alpha}\rho_{\alpha}}{dt} = -\rho_{\alpha}\nabla\cdot\mathbf{v}_{\alpha} \tag{1}$$

$$\frac{d^{\alpha}\mathbf{v}_{\alpha}}{dt} = \frac{1}{\rho_{\alpha}}\nabla\cdot\boldsymbol{\sigma}_{\alpha} + \mathbf{b} \tag{2}$$

where the subscript α denotes the phases, including soil phase, *s*, and water phase, *w*, $\mathbf{v}$ represents the velocity, ρ indicates the density, $\mathbf{b}$ is the external body force, and $\boldsymbol{\sigma}$ denotes the Cauchy stress tensor.

2.2. Pore water flow equation

To model the pore water flow and resolve the pore water pressure in the soil phase, the *u-w-p* form of Biot's theory for unsaturated/saturated porous material is adopted. The advantage of using the *u-w-p* formulation over alternative formulations, such as the *u-p* form, in this application is its completeness in capturing the full dynamic response of soils. By explicitly solving for the relative water velocity (*w*), the *u-w-p* formulation accounts for water acceleration and inertia, which are critical for accurately modelling such transient phenomena as treated in this study and other processes like earthquake-induced liquefaction and wave propagation. In contrast, the *u-p* formulation neglects these terms and is therefore only suitable for slow, quasi-static problems. Moreover, the *u-w-p* formulation helps to mitigate pressure instabilities that may arise in explicit *u-p* frameworks (Lei et al., 2020), avoids the second derivative calculation and its associated issues in SPH approximation of Laplacian operator (Asai et al., 2023), and simplifies the implementation of flux boundary conditions such as rainfall infiltration.

The pore water pressure p_w (linked with density ρ_w for consistency with the free water) and the seepage discharge $\mathbf{q}_w$ in the soil phase are calculated according to (Feng et al., 2022),

$$\frac{d^{s}\rho_{w}}{dt} = -\left(S_w - \frac{\partial S_w}{\partial p_c}K_w\right)^{-1}\frac{\rho_w}{\phi}\left(\nabla\cdot\mathbf{q}_w + S_w\nabla\cdot\mathbf{v}_s\right) \tag{3a}$$

$$\mathbf{q}_w = \frac{K}{g}\left(-\frac{1}{\rho_w}\nabla p_w + \mathbf{b} - \mathbf{a}_s\right) \tag{3b}$$

where S_w is the degree of saturation, p_c is the suction pressure, which is defined as the pressure difference between the pore-air and pore-water, i.e., $p_c = p_a - p_w$, when soil is unsaturated $S_w < S_{w.\max}$. In the present analysis, the air pressure in soils is assumed to be zero, and the air density in the pore space is considered constant for simplification (e.g., Lian et al., 2023; Feng et al., 2024a). K_w is the water bulk modulus, ϕ is the porosity, K is the hydraulic conductivity, $\mathbf{a}_s$ is the soil acceleration $d\mathbf{v}_s/dt$, and g is the magnitude of gravity. The seepage discharge $\mathbf{q}_w$ is defined as $\mathbf{q}_w = \phi S_w(\mathbf{v}_w - \mathbf{v}_s)$.

2.3. Constitutive model

2.3.1. Sub-closure model for water

The Cauchy stress tensor for the water phase comprises of two parts,

$$\boldsymbol{\sigma}_w = -p_w\mathbf{I} + \boldsymbol{\tau} \tag{4}$$

where $\boldsymbol{\tau}$ is the viscous stresses. In this work, the viscous diffusion is considered and the momentum equation for water phase is rewritten as,

$$\frac{d^w\mathbf{v}_w}{dt} = \frac{1}{\rho_w}\nabla p_w + \boldsymbol{\Gamma} + \mathbf{f} \tag{5}$$

in which $\boldsymbol{\Gamma}$ is the diffusive term due to viscosity.

The pressure p_w is related to density variation under the weakly compressible assumption, and the following linear relationship is adopted to calculate the pressure,

$$p_w = \frac{K_w}{\rho_{w0}}(\rho_w - \rho_{w0}) \tag{6}$$

where ρ_{w0} is the initial density of the water.

2.3.2. Suction-dependent soil constitutive model

To account for the influence of soil saturation, the stress tensor for the soil phase is calculated using Bishop's effective stress concept, according to,

$$\boldsymbol{\sigma}_s = \boldsymbol{\sigma}_s' - S_w p_w\mathbf{I} \tag{7}$$

where $\boldsymbol{\sigma}'_s$ is the effective stress tensor that is computed from the soil constitutive model. The value of p_w is evaluated on the soil phase using Eqs. (3a) and (3b), while S_w is determined from the hydraulic constitutive model described in Section 2.3.3.

This study models the mechanical response of soils using an elastic-plastic framework (Zhou et al., 2022, 2025), in which the stress increment $d\boldsymbol{\sigma}'_s$ is calculated from the strain increment $d\boldsymbol{\varepsilon}$ according to,

$$d\boldsymbol{\sigma}_s' = \mathbf{D}^{\mathrm{ep}}d\boldsymbol{\varepsilon} - d\boldsymbol{\omega}\cdot\boldsymbol{\sigma}_s' + \boldsymbol{\sigma}_s'\cdot d\boldsymbol{\omega} \tag{8}$$

where $\mathbf{D}^{\mathrm{ep}}$ represents the elasto-plastic stiffness, $\boldsymbol{\varepsilon}$ denotes the strain tensor, and $\boldsymbol{\omega}$ denotes the spin tensor. The Jaumann stress rate of Cauchy stress tensor is employed to preserve the objectivity of stress under rigid body rotations. $\dot{\boldsymbol{\varepsilon}}$ and $\dot{\boldsymbol{\omega}}$ are calculated from the velocity gradient using the kinematic relations given by,

$$\dot{\boldsymbol{\varepsilon}} = \frac{1}{2}\left(\nabla\mathbf{v} + (\nabla\mathbf{v})^T\right) \tag{9a}$$

$$\dot{\boldsymbol{\omega}} = \frac{1}{2}\left(\nabla\mathbf{v} - (\nabla\mathbf{v})^T\right) \tag{9b}$$

The elastic–plastic constitutive model with suction-dependent strength and strain softening, as introduced by Lian et al. (2024), is adopted to simulate the soil behaviour under different saturation conditions. The adopted constitutive model provides a simple but effective representation of unsaturated soil behaviour (i.e. suction-dependent shear strength, strain softening). To capture other distinctive unsaturated soil behaviour such as wetting-induced volume change or collapse, advanced constitutive models (Ng et al., 2020; Nguyen et al., 2025) are required, and they can be readily implemented in the proposed framework. Herein, only the essential formulations are provided in the following, while further details can be referred to Lian et al. (2024).

The adopted elastoplastic framework is defined by the Drucker-Prager yield criterion (f) and a non-associated plastic potential function (g), which are formulated as follows,

$$f = \alpha_\varphi I_1 + \sqrt{J_2} - k_c, \tag{10a}$$

$$g = \alpha_\psi I_1 + \sqrt{J_2}, \tag{10b}$$

where I_1 and J_2 are respectively the first principal and second deviatoric stress invariants; α_φ and k_c are model constants that are related to cohesion c and friction angle φ according to,

$$\alpha_\varphi = \frac{\tan\varphi}{\sqrt{9 + 12\tan^2\varphi}}, \tag{11a}$$

$$k_c = \frac{3c}{\sqrt{9 + 12\tan^2\varphi}}, \tag{11b}$$

and, α_ψ is a dilatancy factor whose value is related to the dilation angle ψ in the same form as that of α_φ with friction angle φ.

The strength parameters are formulated to account for the contribution of suction pressure, given by,

$$c = c_r' + \left(c_p' - c_r'\right)e^{-\eta\kappa} + c_s, \tag{12a}$$

$$\varphi = \varphi_r' + \left(\varphi_p' - \varphi_r'\right)e^{-\eta\kappa} + \varphi_s, \tag{12b}$$

where c'_p and c'_r are the peak and residual effective cohesion, respectively, φ'_p and φ'_r are the peak and residual effective friction angle, respectively. η is the softening coefficient that control the degradation rate of strength parameters. κ is the equivalent deviatoric plastic strain. c_s and φ_s are respectively the acquired cohesion and friction angle by suction, given by,

$$c_s = c_{sp}\left(1 - e^{-B_s\left(\frac{p_c}{p_{atm}}\right)}\right) \tag{13a}$$

$$\varphi_s = A_s\left(\frac{p_c}{p_{atm}}\right) \tag{13b}$$

where c_{sp} is the maximum additional cohesion provided by suction. A_s and B_s are rate coefficients determining the suction-dependency of the friction angle and cohesion. p_{atm} is the atmosphere pressure, typically taken as 101 kPa.

2.3.3. Soil-water characteristic curve model

To close the governing equations, the constitutive relationship between the degree of saturation S_w and suction pressure p_c is required. This link is defined by the soil-water characteristic curve (SWCC) model. In present analysis, the Van Genuchten model is adopted, defined as,

$$S_w = S_{w.\min} + (S_{w.\max} - S_{w.\min})\left[1 + \left(\frac{p_c}{p_{ref}}\right)^{\frac{1}{1-\lambda}}\right]^{-\lambda} \tag{14}$$

where $S_{w.\min}$ and $S_{w.\max}$ correspond to the residual and maximum saturation levels, respectively, λ and p_{ref} are the fitting parameters.

The permeability of unsaturated soils varies with the water content in the pore spaces. To describe this saturation-dependent permeability, the relative hydraulic conductivity K_{rel} is used, defined as $K_{rel} = K/K_{sat}$,

where K_{sat} is the saturated hydraulic conductivity. The hydraulic conductivity model employed in this work is expressed as,

$$K_{rel} = \sqrt{S_e}\left[1 - \left(1 - S_e^{1/\lambda}\right)^{\lambda}\right]^2 \tag{15}$$

where S_e represents the effective degree of saturation, calculated as $S_e = (S_{w.\max} - S_w)/(S_{w.\max} - S_{w.\min})$.

3. Multiphase SPH formulations

3.1. SPH fundamentals

As a Lagrangian method, SPH discretizes the continuum into a set of moving computational nodes, which are often referred to as particles. Each particle carries physical quantities and evolves according to the governing equations. Since no computational mesh is used, SPH employs point-based interpolation. The value of a physical field at a position $\mathbf{x}$ is computed using a differentiable, compactly supported kernel function W. The SPH interpolation is performed in two steps: integral approximation followed by discrete approximation. The integral approximation of a field function $f(\mathbf{x})$ at the point $\mathbf{x}$ is expressed as,

$$\langle f(\mathbf{x})\rangle = \int_{\Omega} f(\mathbf{x}')W(\mathbf{x}-\mathbf{x}',h)d\mathbf{x}' \tag{16}$$

where Ω denotes the local interpolation region, and $\langle\ldots\rangle$ indicates the SPH interpolation.

The discrete form of Eq. (16) is given by,

$$\langle f(\mathbf{x})\rangle_i = \sum_{j=1}^{N} f(\mathbf{x}_j)W(\mathbf{x}_i-\mathbf{x}_j,h)V_j \tag{17}$$

where the subscript i and j refer to the interpolating particle and its neighbours, respectively, N is the particle numbers in the interpolation domain and V_j is the volume associated to particle j.

For the gradient of a function $\nabla f(\mathbf{x})$, its integral approximation in SPH is given by,

$$\langle \nabla f(\mathbf{x})\rangle = \int_{\Omega} \nabla f(\mathbf{x}')W(\mathbf{x}-\mathbf{x}',h)d\mathbf{x}' \tag{18}$$

and its discrete approximation reads

$$\langle \nabla f(\mathbf{x})\rangle_i = -\sum_{j=1}^{N} f(\mathbf{x}_j)\nabla W(\mathbf{x}_i-\mathbf{x}_j,h)V_j \tag{19}$$

For further details on SPH approximations of different differential operators, including gradient, divergence, and Laplacian operators, the reader is referred to Violeau and Rogers (2016).

In this work, the 5th-order Wendland kernel C^2, which is stable against clumping instability, is adopted. The kernel function is defined as,

$$W(q,h) = \begin{cases} \alpha_d\left(1-\frac{q}{2}\right)^4(2q+1) & 0 \le q \le 2 \\ 0 & q > 2 \end{cases} \tag{20}$$

where the normalization factor α_d is set to $3/4\ h$, $7/(4\pi h^2)$, and $21/(16\pi h^3)$ for one-, two-, and three- dimensions, respectively; and $q = |\mathbf{x} - \mathbf{x}'|/h$ defines the dimensionless separation between points $\mathbf{x}$ and $\mathbf{x}'$.

3.2. Multiphase SPH model

One of the main branches of the multiphase SPH model is to adopt the equations for the evolution of particle volumes to treat the density discontinuity across different phases (Grenier et al., 2009; Hammani et al., 2020). The idea is to associate a particle volume for each SPH particle and to calculate its evolution due to particle movement for the mitigation of the potential sharp density gradient that is often involved in multiphase model. The particle volume is calculated as (Hammani et al., 2020),

$$\left\langle \frac{dV}{dt}\right\rangle_i = V_i\sum_{j=1}^{N} V_j\left(v_j^{\alpha} - v_i^{\alpha}\right)\frac{\partial W_{ij}}{\partial x_i^{\alpha}} \tag{21}$$

in which the equations are written in indicial notation, with the Einstein summation convention applied to repeated indices for clarity.

In this work, the concept of particle volume is adopted but in a different manner, whereby the numerical density is introduced instead of explicitly solving for particle volume. This treatment ensures consistency in density evolution when applying corrections to the density field, such as incorporating density diffusion into the continuity equation. In the present formulation, each particle is associated with a numerical density, which increases or decreases as particles cluster or separate. A constant mass is assigned to each particle according to the relation $m_i = \rho_{i0}V_{i0}$. The equation for numerical density is given by,

$$\left\langle \frac{d\rho}{dt}\right\rangle_i = \rho_i\sum_{j=1}^{N}\frac{m_j}{\rho_j}\left(v_i^{\alpha} - v_j^{\alpha}\right)\frac{\partial W_{ij}}{\partial x_i^{\alpha}} \tag{22}$$

Each particle, regardless of phase, is assigned the same initial numerical density, which then evolves during computation. This approach avoids issues associated with density discontinuities when evaluating contributions from other phases at interphase interfaces (Hammani et al., 2020). In current study, the initial numerical density is taken as the same value of the water phase.

3.2.1. SPH governing equations for water phase

In weakly compressible SPH schemes for water flow, high-frequency oscillations and noise often appear in the pressure field. To mitigate this issue, the δ-SPH scheme by Marrone et al. (2011) and Antuono et al. (2012) is applied to the water phase. This approach introduces diffusive terms into both the continuity and momentum equations. The added momentum diffusion has physical meaning and can be related to the kinematic viscosity according to Monaghan (2005). The SPH-discretized forms of the governing equations for the water phase are given as follows,

$$\left\langle \frac{d^w\rho_w}{dt}\right\rangle_i = \rho_{wi}\sum_{j=1}^{N}\frac{m_j}{\rho_j}\left(v_i^{\alpha} - v_j^{\alpha}\right)\frac{\partial W_{ij}}{\partial x_i^{\alpha}} + \delta h c_{w0}\sum_{j=1}^{N}\frac{m_j}{\rho_j}\psi_{\rho w.ij}^{\alpha}\frac{\partial W_{ij}}{\partial x_i^{\alpha}} \tag{23a}$$

$$\left\langle \frac{d^w v_w^{\alpha}}{dt}\right\rangle = \frac{1}{\rho_{wi}}\sum_{j=1}^{N}\frac{m_j}{\rho_j}\left(p_{wi}+p_{wj}\right)\frac{\partial W_{ij}}{\partial x_i^{\alpha}} + \alpha_{\mu.w}c_{w0}h\sum_{j=1}^{N}\frac{m_j}{\overline{\rho}_{ij}}\mu_{ij}\frac{\partial W_{ij}}{\partial x_i^{\alpha}} + g_i^{\alpha} \tag{23b}$$

where the subscript ij represents a pairwise difference in the function $f_{ij} = f_i - f_j$; δ is the the dimensionless diffusion coefficient, typically taken as $\delta = 0.1$ (Marrone et al., 2011); $\alpha_{\mu.w}$ is the constant governing the magnitude of viscous dissipation in water, and its value is normally taken as $\alpha_{\mu.w} = 0.01$ (Altomare et al., 2015); c_{w0} is the numerical speed of sound for water, and its value can be selected according to (Sun et al., 2019),

$$c_{w0} \ge 10\max\left(v_{w.\max}, \sqrt{\frac{p_{\max}}{\rho_{w0}}}\right) \tag{24a}$$

in which $v_{w.\max}$ and Δp_{max} are respectively maximum expected velocity and pressure variation in the water phase. $\overline{\rho}_{ij}$ is the mean particle density, defined as $\overline{\rho}_{ij} = (\rho_i + \rho_j)/2$; $\psi_{\rho w.ij}^{\alpha}$ and μ_{ij} are respectively the density diffusive term and viscosity diffusive term that are calculated as,

$$\psi_{\rho w.ij}^{\alpha} = 2\left(\rho_{w.i} - \rho_{w.j}\right)\frac{x_{ij}^{\alpha}}{x_{ij}^{\alpha}x_{ij}^{\alpha} + \eta^2} - \left(\langle\partial\rho_w/\partial x^{\alpha}\rangle_j^L + \langle\partial\rho_w/\partial x^{\alpha}\rangle_i^L\right) \tag{24b}$$

$$\mu_{ij} = \begin{cases} \dfrac{v_{ij}^{\alpha} x_{ij}^{\alpha}}{x_{ij}^{\alpha} x_{ij}^{\alpha} + \eta^2} & v_{ij}^{\alpha} x_{ij}^{\alpha} < 0 \\ 0 & v_{ij}^{\alpha} x_{ij}^{\alpha} \geq 0 \end{cases} \tag{24c}$$

in which η, set to 0.1 h, is a small constant added to maintain numerical stability and prevent the calculation from singularity. $\langle \partial \rho_w / \partial x^{\alpha} \rangle^L$ is the renormalized density gradient defined as

$$\langle \partial \rho_w / \partial x^{\alpha} \rangle_i^L = \sum_j \frac{m_j}{\rho_j} (\rho_{w.j} - \rho_{w.i}) L_i^{\alpha\beta} \frac{\partial W_{ij}}{\partial x_i^{\beta}} \tag{25a}$$

$$L_i^{\alpha\beta} = \left(- \sum_j \frac{m_j}{\rho_j} \left(x_j^{\beta} - x_i^{\beta} \right) \frac{\partial W_{ij}}{\partial x_i^{\alpha}} \right)^{-1} \tag{25b}$$

3.2.2. SPH governing equations of soil phase

In the soil phase, the continuity equation is transformed into a porosity equation, while the density of soils is obtained from mixture theory to account for water saturation (Feng et al., 2024a). Similar to the water phase, an artificial diffusive term is included in the momentum equation to mitigate high-frequency oscillations caused by the collocated nature of the SPH method (Bui and Nguyen, 2021). The δ-SPH scheme is extended to the governing equation for pore water flow. The SPH discretisation of the governing equations for the soil phase are given by:

$$\left\langle \frac{d^s \phi}{dt} \right\rangle_i = (1 - \phi_i) \dot{\varepsilon}_{v.i} \tag{26a}$$

$$\left\langle \frac{d^s v_s^{\alpha}}{dt} \right\rangle = \frac{1}{\rho_{si}} \sum_{j=1}^{N} \frac{m_j}{\rho_j} \left(\sigma_{si}^{\alpha\beta} + \sigma_{sj}^{\alpha\beta} \right) \frac{\partial W_{ij}}{\partial x_i^{\beta}} + \alpha_{\mu.s} c_{s0} h \sum_{j=1}^{N} \frac{m_j}{\bar{\rho}_{ij}} \mu_{ij} \frac{\partial W_{ij}}{\partial x_i^{\alpha}} + g_i^{\alpha} \tag{26b}$$

$$\langle \dot{\varepsilon}^{\alpha\beta} \rangle_i = \frac{1}{2} \left(\sum_{j=1}^{N} \frac{m_j}{\rho_j} \left(v_j^{\alpha} - v_i^{\alpha} \right) \frac{\partial W_{ij}}{\partial x_i^{\beta}} + \sum_{j=1}^{N} \frac{m_j}{\rho_j} \left(v_j^{\beta} - v_i^{\beta} \right) \frac{\partial W_{ij}}{\partial x_i^{\alpha}} \right) \tag{26c}$$

$$\langle \dot{\omega}^{\alpha\beta} \rangle_i = \frac{1}{2} \left(\sum_{j=1}^{N} \frac{m_j}{\rho_j} \left(v_j^{\alpha} - v_i^{\alpha} \right) \frac{\partial W_{ij}}{\partial x_i^{\beta}} - \sum_{j=1}^{N} \frac{m_j}{\rho_j} \left(v_j^{\beta} - v_i^{\beta} \right) \frac{\partial W_{ij}}{\partial x_i^{\alpha}} \right) \tag{26d}$$

the discretised equations of Eqs. (3a) and (3b) for the pore water flow in the soil phase are given by,

$$\left\langle \frac{d^s \rho_w}{dt} \right\rangle_{i \in S} = - \frac{1}{C_{ri}} \left[\rho_{wi} \left(\sum_{j=1}^{N} \frac{m_j}{\rho_j} \left(q_{wj}^{\alpha} - q_{wi}^{\alpha} \right) \frac{\partial W_{ij}}{\partial x_i^{\alpha}} + S_{wi} \dot{\varepsilon}_{v.i} \right) + \delta h c_{pw0} \sum_{j=1}^{N} \frac{m_j}{\rho_j} \psi_{\rho w.ij}^{\alpha} \frac{\partial W_{ij}}{\partial x_i^{\alpha}} \right], \tag{27a}$$

$$\langle q_w^{\alpha} \rangle_{i \in S} = \frac{K_i}{g} \left(- \frac{1}{\rho_{w.i}} \sum_{j=1}^{N} \frac{m_j}{\rho_j} \left(p_{w.j} - p_{w.i} \right) \frac{\partial W_{ij}}{\partial x_i^{\alpha}} + g_i^{\alpha} - a_{si}^{\alpha} \right) \tag{27b}$$

where

$$\rho_s = (1 - \phi) \rho_{s0} + S_w \phi \rho_{w0} \tag{28a}$$

$$C_r = \phi \left(S_w - K_w \frac{\partial S_w}{\partial p_c} \right) \tag{28b}$$

μ_{ij} and $\psi_{\rho w.ij}^{\alpha}$ are respectively the viscous stabilization term and density diffusive term for the soil deformation and pore water flow, which takes the same formulation as those in the water phase expressed in Eqs. (24a) and (24b); $\alpha_{\mu.s}$ is the constant controlling the magnitude of momentum diffusion in soils, and its value is normally taken as $\alpha_{\mu.s} = 0.1$ (Bui and Nguyen, 2021); c_{pw0} is the numerical speed of sound for pore water, given by $c_{pw0} \geq 10 q_{w.max}$.; c_{s0} is the speed of sound of the soil, which is calculated by,

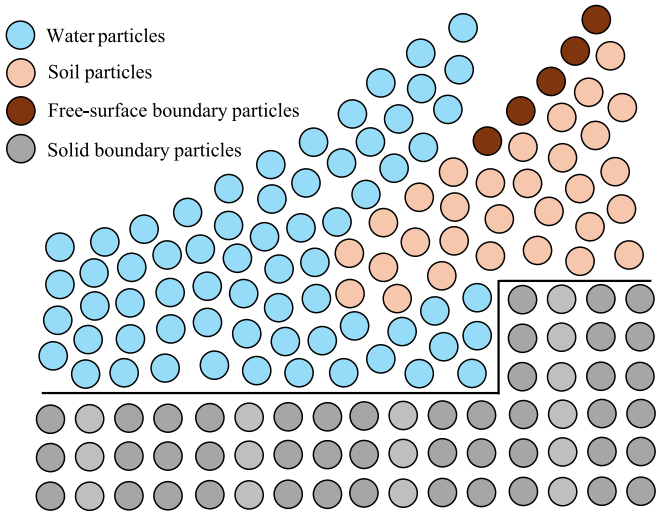

Fig. 1. Illustrative diagram of the boundary treatment and associated particle classifications.

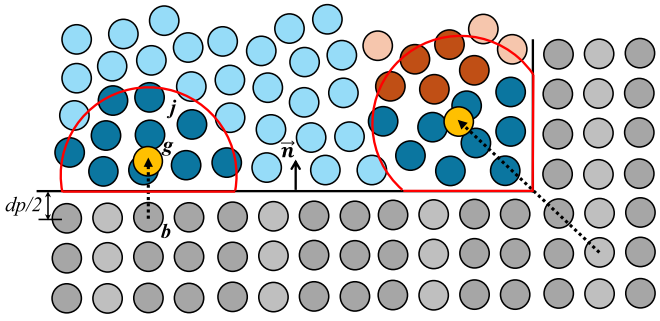

Fig. 2. Illustrative diagrams of the solid boundary treatment.

$$c_{s0} = \sqrt{(4G/3 + K)/\rho_{s0}} \tag{29}$$

in which K and G are respectively bulk modulus and shear modulus of the soil.

It is noted that, unlike the established SPH scheme for the coupled flow-deformation problem in saturated/unsaturated porous materials (e.g., Lian et al., 2024; Feng et al., 2024a), where gradient correction technique is applied for SPH modelling of pore water flow, in this study the δ-SPH scheme with standard SPH operator is adopted, which allows an unified description of both free water flow and pore water flow. Previous study by Feng et al. (2024a) has shown that the inclusion of the diffusion term into pore water equation can effectively smooth out the

numerical noise in pore pressure prediction and stabilise numerical simulation. Validation cases presented in Section 4 confirm the accuracy of the proposed method.

3.3. Boundary conditions

Two general types of boundary conditions are needed for the simulation of multi-hazard cascades from their triggering, including solid boundaries and free-surface boundaries. Solid boundary condition is a common type of boundary for both soil phase and water phase as the physical limits of the simulation domain, for example, representing nearly non-deformable ground layers with very low permeability (such as bedrock) or specified hydraulic conditions (such as a given groundwater level). Free-surface boundary conditions are another essential component to model pore water flow in the soil phase, for example in cases of water infiltrations due to rainfall or when a specific hydraulic pressure condition is prescribed. Fig. 1 shows the illustrative diagram of the adopted particle-based boundary treatments together with associated particle types. For soil particles submerged in water, due to the solution of Eq. (23b), pressure condition from the water phase is naturally enforced at the soil-water interface.

3.3.1. Solid boundary condition

In this work, the particle-based solid boundary treatment for coupled soil–water problems proposed by Feng et al. (2022) is adopted and extended to three-dimensional applications. As shown in Fig. 2, several layers of dummy boundary particles, *b*, are introduced to complete the kernel support for particles truncated by the solid boundary. For each boundary particle, ghost nodes, *g*, are mirrored into the computational domain to enable interpolation of field variables.

The values and gradients of the field variables at ghost particles are evaluated using the first-order consistent correction introduced by Liu and Liu (2006), given by

$$A_g \cdot \begin{bmatrix} \sigma_g^{\alpha\beta} \\ \partial_x \sigma_g^{\alpha\beta} \\ \partial_y \sigma_g^{\alpha\beta} \\ \partial_z \sigma_g^{\alpha\beta} \end{bmatrix} = \begin{bmatrix} \sum_j \sigma_j^{\alpha\beta} W_{gj} V_j \\ \sum_j \sigma_j^{\alpha\beta} \partial_x W_{gj} V_j \\ \sum_j \sigma_j^{\alpha\beta} \partial_y W_{gj} V_j \\ \sum_j \sigma_j^{\alpha\beta} \partial_z W_{gj} V_j \end{bmatrix} \tag{30}$$

where the renormalisation matrix $\mathbf{A}_g$ is given by,

$$A_g = \begin{bmatrix} \sum_j W_{gj} V_j & \sum_j (x_j - x_g) W_{gj} V_j & \sum_j (y_j - y_g) W_{gj} V_j & \sum_j (z_j - z_g) W_{gj} V_j \\ \sum_j \partial_x W_{gj} V_j & \sum_j (x_j - x_g) \partial_x W_{gj} V_j & \sum_j (y_j - y_g) \partial_x W_{gj} V_j & \sum_j (z_j - z_g) \partial_x W_{gj} V_j \\ \sum_j \partial_y W_{gj} V_j & \sum_j (x_j - x_g) \partial_y W_{gj} V_j & \sum_j (y_j - y_g) \partial_y W_{gj} V_j & \sum_j (z_j - z_g) \partial_y W_{gj} V_j \\ \sum_j \partial_z W_{gj} V_j & \sum_j (x_j - x_g) \partial_z W_{gj} V_j & \sum_j (y_j - y_g) \partial_z W_{gj} V_j & \sum_j (z_j - z_g) \partial_z W_{gj} V_j \end{bmatrix} \tag{31}$$

Based on the interpolated values and gradients of the field variables at the ghost nodes, the final values at the boundary particle ($\boldsymbol{\sigma}_b$ and ρ_{wb}) are extrapolated from the positions of the ghost nodes using a first-order Taylor series expansion, as given by

$$\sigma_b^{\alpha\beta} = \sigma_g^{\alpha\beta} + (x_b - x_g)\partial_x \sigma_g^{\alpha\beta} + (y_b - y_g)\partial_y \sigma_g^{\alpha\beta} + (z_b - z_g)\partial_z \sigma_g^{\alpha\beta} \tag{32a}$$

$$\rho_{wb} = \rho_{wg} + (x_b - x_g)\partial_x \rho_{wg} + (y_b - y_g)\partial_y \rho_{wg} + (z_b - z_g)\partial_z \rho_{wg} \tag{32b}$$

To ensure a sufficient number of neighbouring particles are involved in the boundary extrapolation, the invertibility of the renormalization matrix **Ag** is assessed by computing its determinant. When the determinant is very small (by default, below 0.001) and the matrix becomes ill-conditioned, a zeroth-order consistent SPH interpolant (Shepard function) is employed, given by:

$$\sigma_b^{\alpha\beta} = \sigma_g^{\alpha\beta} = \frac{\sum_j \sigma_j^{\alpha\beta} W_{gj} V_j}{\sum_j W_{gj} V_j} \tag{33a}$$

$$\rho_{wb} = \rho_{wg} = \frac{\sum_j \rho_{wj} W_{gj} V_j}{\sum_j W_{gj} V_j} \tag{33b}$$

For the no-slip boundary condition in both water and soil phase, as well as the impermeable condition of pore water in the soil phase, the velocity and seepage discharge at the ghost nodes are computed by the Shepard-corrected interpolation, defined as,

$$v_g^{\alpha} = \frac{\sum_j v_j^{\alpha} W_{gj} V_j}{\sum_j W_{gj} V_j} \tag{34a}$$

$$q_{wg}^{\alpha} = \frac{\sum_j q_{wj}^{\alpha} W_{gj} V_j}{\sum_j W_{gj} V_j} \tag{34b}$$

To enforce no-slip and no-penetration conditions, each boundary particle is assigned a velocity that is equal in magnitude and opposite in direction to that of its paired ghost node,

$$v_b^{\alpha} = -v_g^{\alpha} \tag{35a}$$

$$q_{wb}^{\alpha} = -q_{wg}^{\alpha} \tag{35b}$$

3.3.2. Hydraulic boundary condition

3.3.2.1. Solid boundary condition. In the scenario of simulating groundwater levels, a prescribed pressure boundary condition for the pore water flow as well as the no-penetration solid boundary condition for the soil movement are required. The solid boundary treatment presented in Section 3.3.1 is extended to enable the imposition of pressure conditions on the solid boundary. The water density at boundary particles is then expressed as,

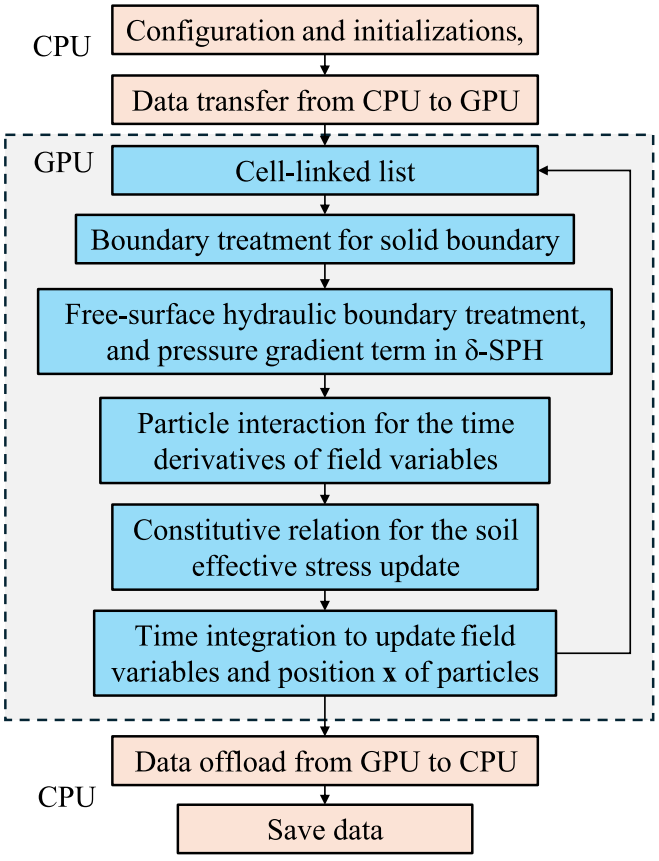

Fig. 3. Solution procedures for the multiphase soil-water SPH model.

$$\rho_{wb} = 2\rho_{w.pres} - \rho_{wg} \tag{36a}$$

$$\rho_{w.pres} = \rho_{w0}\left(1 + p_{w.pres}\big/K_w\right) \tag{36b}$$

where $p_{w.pres}$ is the prescribed pressure condition.

As the pressure condition is imposed, the velocity condition at boundary particles is not constrained and is instead assigned the same value as at the ghost nodes, given by

$$q^{\alpha}_{wb} = q^{\alpha}_{wg} \tag{37}$$

3.3.2.2. Free-surface boundary condition. The treatment of free-surface boundaries is based on the method developed by Feng et al. (2024a), which is extended for use in three-dimensional problems in this work. This boundary treatment is required for scenarios such as rainfall infiltration where a specific hydraulic condition should be enforced on the free surface of soil phase with the given infiltration intensity. The first step of the method is to locate particles on the free surface by calculating their position divergence. Specifically, a particle i is marked as a free-surface particle (*i-FS*) if its position divergence satisfies the condition $\nabla\cdot\mathbf{x} < FST$, where the free surface threshold (*FST*) is set to 1.5 in two dimensions and 2.5 in three dimensions. This identification technique, while straightforward, is proven to be effective and has seen successful application in previous work (e.g., Mokos et al., 2017; Feng et al., 2024a, 2024b). The position divergence is computed in SPH according to,

$$\langle\nabla\cdot\mathbf{x}\rangle_i = \sum_j \frac{m_j}{\rho_j}\left(x^{\alpha}_i - x^{\alpha}_j\right)\frac{\partial W_{ij}}{\partial x^{\alpha}_i} \tag{38}$$

After the free-surface detection, prescribed hydraulic conditions (e.g., seepage flux or pressure) are imposed on free-surface particles as Dirichlet boundary conditions, given by

$$q^{\alpha}_{w.i-FS} = q^{\alpha}_{w.pres} \text{ or } p_{w.i-FS} = p_{w.pres} \tag{39}$$

To realistically simulate infiltration, the model incorporates an adaptive boundary strategy at the free surface. The boundary region is initially prescribed with a specified seepage flux. However, when the flux exceeds the absorption capacity of soils, ponding occurs. At that point, the prescribed flux is replaced by a fixed pressure condition with the maximum allowable pressure, i.e., $P \le P_{\max}$. A similar adjustment is made during desaturation: when the soil dries and reaches its limit, the pressure boundary condition is activated to impose the minimum allowable pressure, i.e., $P > P_{\min}$.

It is noted that the proposed boundary framework can be extended to model other triggering mechanisms, including human activities, earthquakes, and water-level changes. For instance, reservoir water-level changes and human activities can be simulated by generalizing the free-surface boundary into the general hydraulic-mechanical boundary approach of Feng et al. (2024a). Seismic analysis can be performed by converting base acceleration-time histories to stress-time histories via the method of Hoang et al. (2024) and applying them through the solid boundary treatment to input seismic motions. The generalization of these developments for broader scenarios will be the focus of future work.

3.4. Time integration scheme

The Symplectic Position Verlet scheme is adopted for the time integration of the governing equations, Eq. (22), Eqs. (23a), (23b), (26a)–(26d), and (27a), (27b). This scheme consists of two substeps per time step and is second-order accurate in time. For a comprehensive description of the time integration scheme employed here, the reader is referred to Domínguez et al. (2022). The variable time step is determined using the formulation from Feng et al. (2022), which is constrained by three criteria: the Courant-Friedrichs-Lewy (CFL) condition, the maximum force term, and the pore water diffusion rate, given by,

$$\Delta t_f = \min_i\left(\sqrt{h/\|\mathbf{f}_i\|}\right) \tag{40a}$$

$$\Delta t_{cv} = \min_i \frac{h}{\max(c_{s0}, c_{w0}) + \max_j\left|\frac{h\mathbf{v}_{ij}\cdot\mathbf{x}_{ij}}{\mathbf{x}^2_{ij}+\eta^2}\right|}, \tag{40b}$$

$$\Delta t_{sp} = \min_i\left(\frac{\gamma_w}{K_w}\frac{h^2 c_v}{2K}\right) \tag{40c}$$

$$\Delta t = C_0 \min\left(\Delta t_{cv}, \Delta t_f, \Delta t_{sp}\right) \tag{40d}$$

where

$$c_v = \phi\left(S_w - K_w\frac{\partial S_w}{\partial p_c}\right) \tag{41}$$

$\mathbf{f}$ is the force per unit mass (i.e., the acceleration computed in momentum equation), and C_0 is the Courant number that is taken as 0.2 by default.

3.5. Solution procedures

A unique advantage of a single, unified numerical framework is its streamlined implementation for parallel computing, which avoids the complexities inherent in hybrid methods that often require intricate interface coupling and substantial communication overhead. The new multiphase soil-water SPH model is implemented using the CUDA parallel framework to harness GPU hardware acceleration, enabling its application to large-scale 3D problems. The computational workflow is summarized below and shown in the flowchart in Fig. 3.

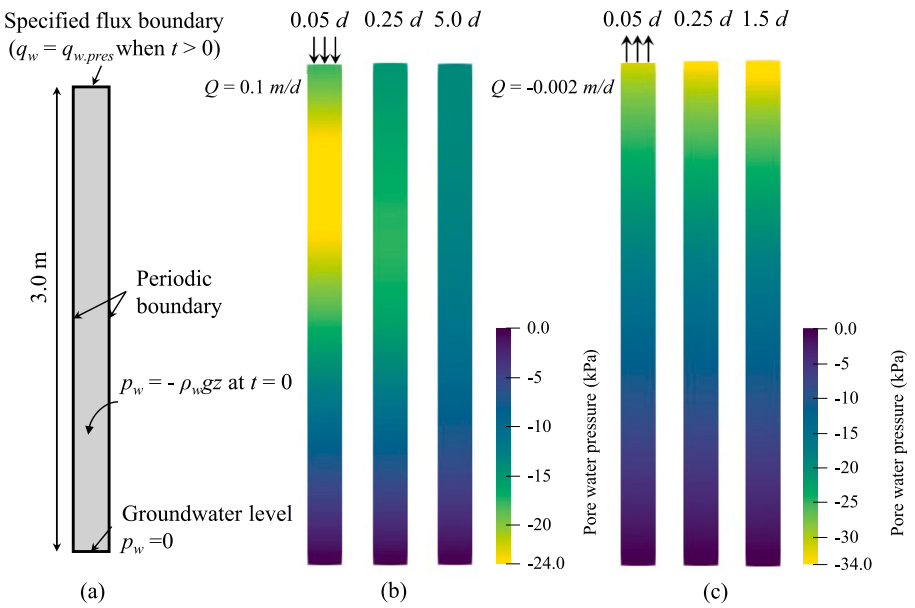

Fig. 4. Transient pore flow in unsaturated porous column: (a) the numerical setup, and the evolution of pore water pressure during (b) infiltration and (c) evaporation.

The solution begins on the CPU. This step involves setting up the entire simulation environment, including defining the geometry of the problem, configuring boundaries, particle classification, initialisation of field variables to all particles, and specifying material properties for both soil and water phases. Once the initial state is configured, all the necessary data is transferred from the host (CPU) memory to the dedicated memory of the Graphics Processing Unit (GPU) to execute the main computational loop.

Within each computational time step on GPU, the SPH solution starts from the construction of a cell-linked list for efficient neighbour searching. This is followed by handling solid boundary for soil and water phase, free-surface identification for hydraulic boundary treatment, and the evaluation of the pressure gradient term in δ-SPH, i.e., Eqs. (25a) and (25b). After this pre-interaction step, particle interactions are performed for evaluating the right-hand side terms of governing equations, i.e., Eq. (22), Eqs. (23a), (23b), (26a)–(26d), and (27a), (27b). Then, time integrations are conducted to update all the field variables as well as the update of soil effective stress described in section 2.3.3. Once the simulation is complete, or at specified intervals for output, the results are transferred back from GPU memory to CPU memory for data storage.

The implementation of the described solution procedure is achieved in GeoDualSPHysics (Feng et al., 2025b), the geomechanics branch of the open-source, CUDA/OpenMP based SPH code DualSPHysics (Domínguez et al., 2022). GeoDualSPHysics employs identical CUDA configuration parameters with DualSPHysics. By default, BlockSize is fixed at 128 threads, but other optimal calculation modes are also available. The number of blocks is determined by dividing the number of particles by the number of threads per block, ensuring that each particle is assigned to a thread. Shared memory is used selectively within CUDA kernels, primarily for caching particle information during neighbour searches and for reduction operations, while most particle data reside in global memory due to the large dataset sizes. For details on the CUDA implementation and solver performance, readers are referred to Feng et al. (2025b) and Domínguez et al. (2022).

4. Validation cases

Four benchmark examples are used in this section to validate the performance and accuracy of the proposed numerical scheme, including, 1-D infiltration/evaporation test, Liakopoulos's drainage test, Fei Tsui Road rainfall-induced landslide, and landslide-induced tsunami experiment, with the comparison to the reported solution and data available in the literature.

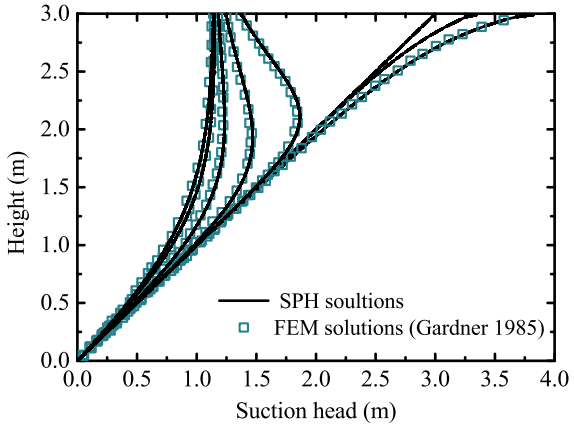

Fig. 5. Comparison of the evolution of suction head between SPH results and reference FEM solutions (Gardner, 1958).

4.1. One-dimensional infiltration/evaporation test

This validation case models the transient flow in an initially unsaturated porous column driven by infiltration and evaporation. The validity of the proposed framework is evaluated by comparing the results to the finite element solutions from Gardner (1958). To ensure a direct comparison, the analysis adopts identical material parameters and numerical configurations to those used in Gardner's original work.

The geometry and configuration of the numerical model are shown in Fig. 4(a). The porous column is 3 m in height and initially partially saturated, with the initial pore water pressure (or matric suction) defined as $p_w = -\rho_w gz$. The column is assumed to be rigid and non-deformable. The lateral boundaries are defined as periodic for creating the 1-D flow condition. Pore flow is initiated by a prescribed vertical flux ($q_{w,z}$) at the top surface; the infiltration scenario adopts a rate of +0.1 m/day, while the evaporation scenario uses −0.002 m/day. At the bottom of the domain, a no-flow condition is enforced by treating it as an

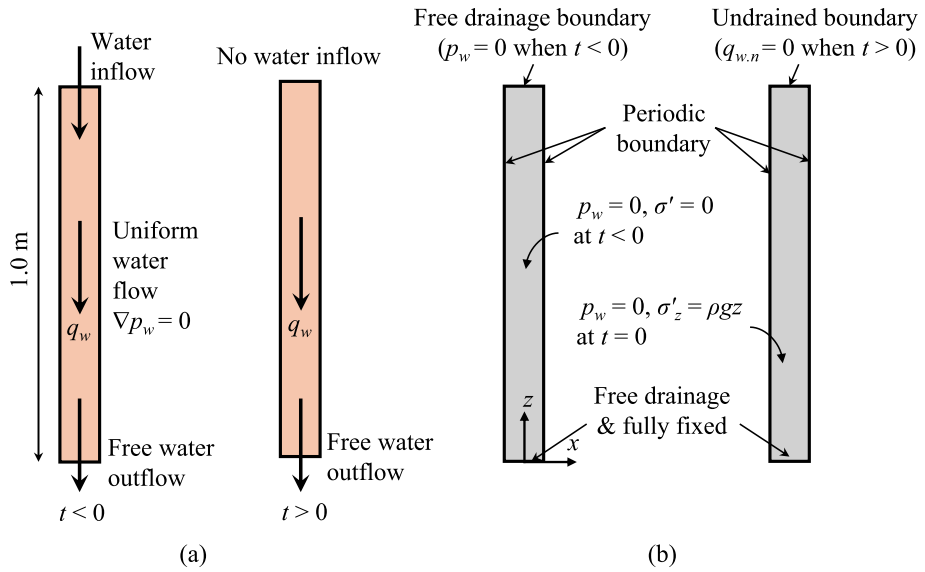

Fig. 6. Coupled flow-deformation in unsaturated porous column: (a) experimental configuration and (b) numerical configuration.

Table 1
Adopted material properties for the Liakopoulos's drainage test.

Parameters	Unit	Value
Soil grain density ρ_{s0}	kg/m^3	2000
Water density ρ_{w0}	kg/m^3	1000
Porosity ϕ	–	0.2975
Water bulk modulus K_w	Pa	2×10^6
Saturated hydraulic conductivity K_{sat}	m/s	4.41×10^{-6}
Young's modulus E	MPa	1.3
Poisson's ratio ν	–	0.4

impermeable layer using the solid boundary treatment. The porosity of the column is taken as 0.4, the hydraulic conductivity is set to $K_{sat} = 1.0$ m/day. The following SWCC model and HCC model are used for the hydraulic constitutive relations,

$$S_w = 0.23 + (1.0 - 0.23)\exp\left(-\frac{2p_c}{\rho_{w0}g}\right) \tag{42a}$$

$$K = K_{sat}\exp\left(-\frac{2p_c}{\rho_{w0}g}\right) \tag{42b}$$

The initial particle spacing is taken as dp = 0.02 m with h/dp = 1.8. A fixed time step $dt = 10^{-5}$ day is adopted.

Fig. 4(b,c) shows the pore water pressure evolution along the height of the unsaturated column caused by infiltration and evaporation. The water flux applied at the top boundary gradually decreases suction during infiltration and increases it during evaporation. The proposed numerical framework effectively captures the wetting and drying processes, producing smooth and noise-free pressure profiles.

Fig. 5 plots the computed pore water pressure profiles against the finite element reference solutions at several time instants. The SPH results are in excellent agreement with the FEM solutions, confirming the method's ability to accurately model transient flow in unsaturated porous media.

4.2. Liakopoulos's drainage test

To validate the proposed scheme for coupled unsaturated flow and solid deformation, the drainage test conducted by Liakopoulos (1964) is simulated in this case. The experimental setup is shown in Fig. 6(a). Initially, a steady-state, uniform water flow is established by applying a constant inflow at the top of the specimen while keeping the bottom drainage open. The test is then initiated by stopping the inflow at the top and allowing the pore water to drain at the bottom due to gravity.

The numerical simulation is consistent with the experimental setup, as shown in Fig. 6(b). An initialization stage of 20 s is performed by applying a zero-pressure boundary at the top using the free-surface boundary treatment, and at the bottom using the solid boundary treatment. This process helps dissipate the initial excess pore water generated by the sudden application of gravity and the resulting solid deformation.

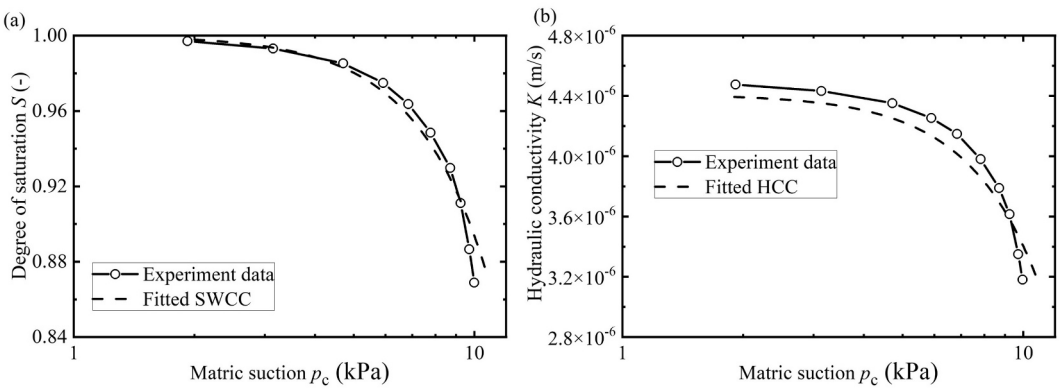

Fig. 7. Plot of the hydraulic model used in simulation: (a) SWCC and (b) HCC.

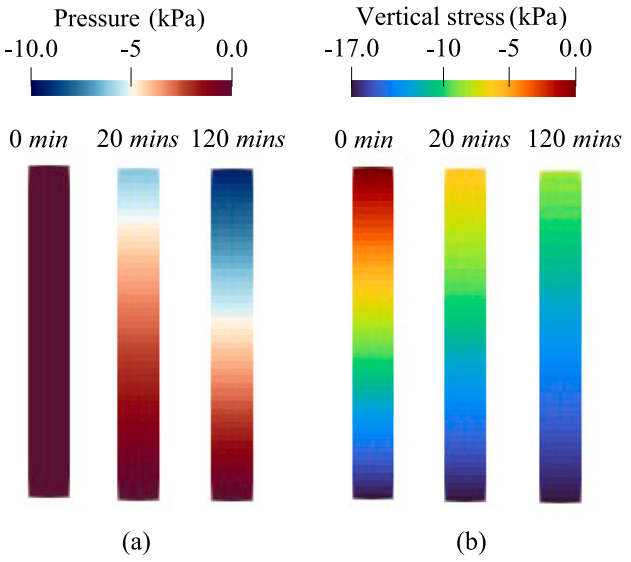

Fig. 8. Evolution of (a) pore water pressure and (b) effective vertical stress due to the gravity-induced drainage.

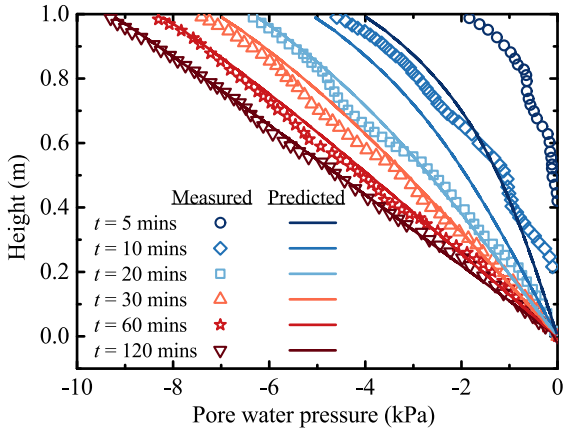

Fig. 9. Comparison of pore water pressure along height between SPH predictions and experiment measurements at different time instants.

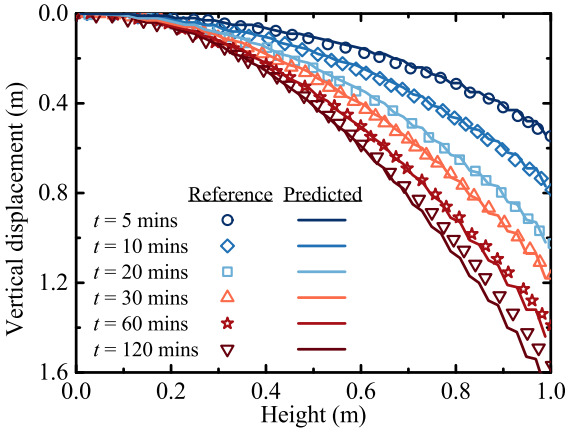

Fig. 10. Comparison of the vertical displacement along height between SPH predictions and the reference results by Wang et al. (2018) at different time instants.

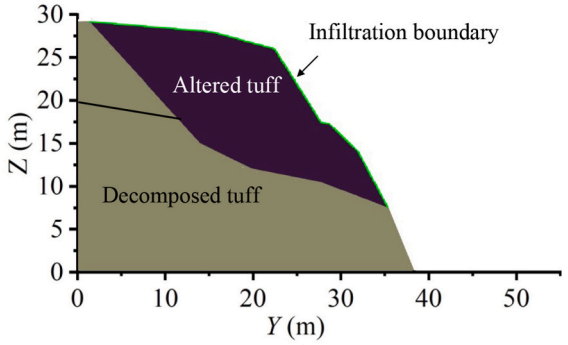

Fig. 11. Rainfall-induced landslide: geometries and boundary condition.

Table 2
Adopted material properties for the rainfall-induced landslide simulation.

Parameters	Unit	Value
Soil grain density ρ_{s0}	kg/m^3	2650
Water density ρ_w	kg/m^3	1000
Porosity ϕ	–	0.3
Water bulk modulus K_w	Pa	2×10^6
Saturated hydraulic conductivity K_{sat}	m/s	1.0×10^{-3}
Maximum degree of saturation $S_{\max}$	–	1.0
Residual degree of saturation $S_{\min}$	–	0.3
SWCC constant λ	–	0.447
SWCC constant p_{ref}	kPa	19.357
Young's modulus E	MPa	50
Poisson's ratio ν	–	0.3
Peak cohesion c_p	kPa	10
Residual cohesion c_r	kPa	3
Peak friction angle φ_p	°	34
Residual friction angle φ_r	°	32
Strain-softening coefficient η	–	1
Suction-hardening coefficient A_s	°	0
Suction-hardening coefficient B_s	–	10
Suction-dependent cohesion c_{s0}	kPa	10

After initialization, a zero pore-water pressure and the corresponding static stress profile are obtained. The top boundary is then set to undrained to initiate the drainage simulation.

The linear elastic model is adopted to simulate solid deformation. The hydraulic constitutive relations for SWCC and HCC are described using,

$$S_w = 1.0 - 0.10152\left(\frac{p_c}{\rho_{w0}g}\right)^{2.4279} \tag{43a}$$

$$K = K_{sat}\left(1.0 - 2.207(1.0 - S_w)^{1.0121}\right) \tag{43b}$$

The material properties are taken from Schrefler and Scotta (2001) and Bandara et al. (2016) and are listed in Table 1. Fig. 7 plots the resulting fitted SWCC and HCC against the experimental data.

The domain height is resolved by 50 particles, with an initial spacing of 0.02 m. In addition to the described stabilization techniques, the viscous dissipation term proposed by Feng et al. (2024b) with a viscous coefficient of 0.1 is also applied to supress the oscillations in the SPH simulation of elastic materials (e.g., Lian et al., 2023).

Fig. 8 shows the evolution of pore water pressure and effective vertical stress in the simulation of drainage test at different time instants. Drainage at the bottom induces the development of matric suction (or negative pore water pressure) from the top of the column and increases the effective stress in the solid. The proposed method enables a smooth prediction of both pore water pressure and vertical stress. Quantitative comparison of pore water pressure evolution between numerical simulation and experiment measurements is shown in Fig. 9. Overall, the predictions match well with the experimental data. In the first 10 min of

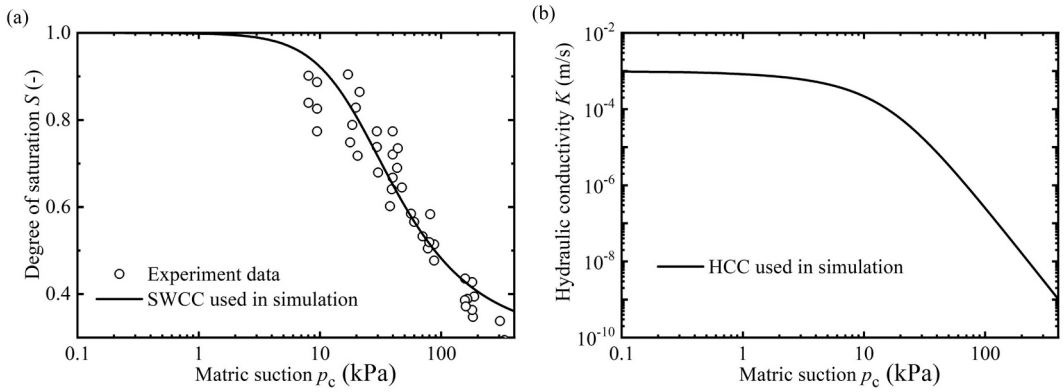

Fig. 12. Plot of the hydraulic model used in simulation: (a) SWCC and (b) HCC.

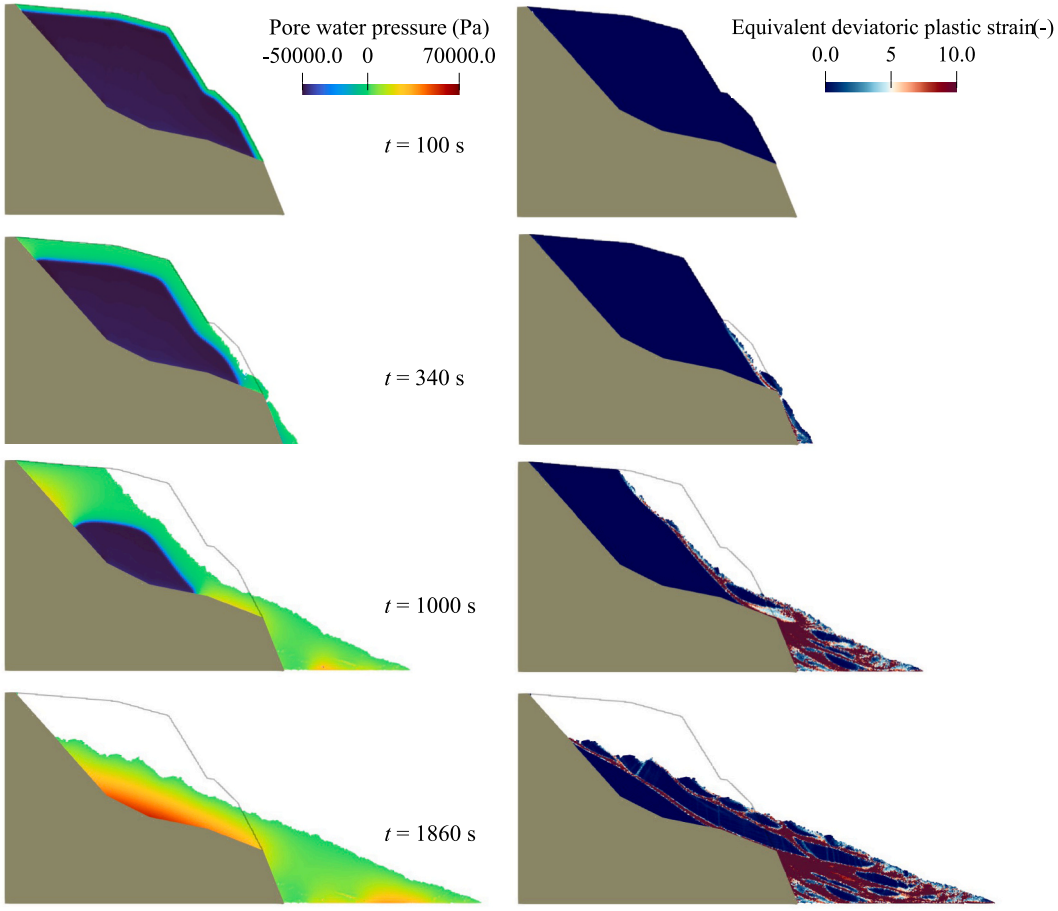

Fig. 13. Evolution of pore water pressure and equivalent plastic strain for the rainfall-induced landslide.

the simulation, however, the predicted pressure overestimates the development of suction pressure measured in the experiment. This discrepancy may be attributed to idealizations in the numerical setup compared with the physical experiments and has also been reported in other numerical studies of the same case, such as FEM (Schrefler and Scotta, 2001) and MPM analyses (Bandara et al., 2016).

Fig. 10 shows the predicted vertical displacement profiles along the height of the column, together with the reference results reported by Wang et al. (2018) for comparison. Changes in effective stress during drainage cause progressive deformation of the soil skeleton over time. The computed evolution of the displacement profile is consistent with the reference data, confirming the validity of the present framework for analysing coupled flow–deformation problems in unsaturated soils.

4.3. *Rainfall-induced landslide*

This case studies the 1995 Fei Tsui Road landslide in Hong Kong, which was triggered by a heavy rainfall following Typhoon Helen. The event is one of the largest recorded landslides on a permanent cut slope in Hong Kong, with a maximum runout distance of 29 m (Knill, 1996). The geometry and configuration of the numerical model are shown in Fig. 11.

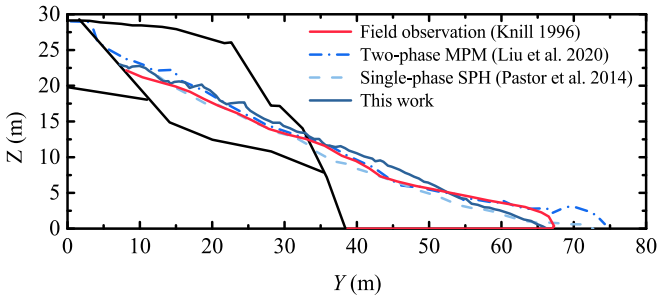

Fig. 14. Comparison of the final deposition profile between numerical simulation and field observation.

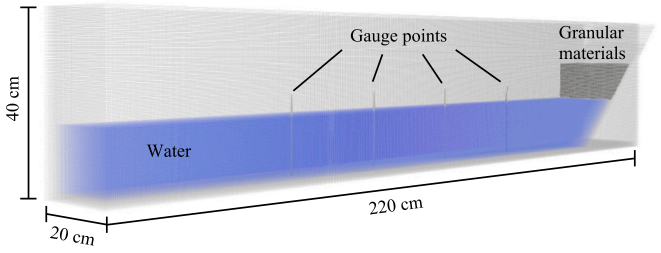

Fig. 15. Landslide-induced tsunami: geometries and numerical configuration.

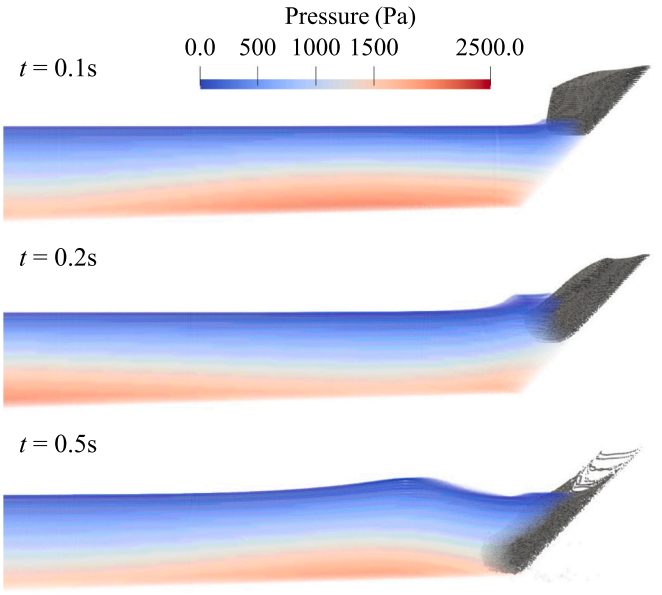

Fig. 16. Evolution of landslide generated waves with the plot of water pressure at different time instants.

The slope consists of an upper layer of altered tuff underlain by slightly, moderately, or highly decomposed tuff. Given the relatively low permeability and negligible seepage flow in the lower soil layer (Liu et al., 2020; Cuomo et al., 2021), they are treated as solid boundaries in the analysis. The boundary condition for water infiltration is imposed on the free surface of the upper soil layers.

Table 2 lists the adopted material properties in the numerical simulation. The mechanical and physical properties of the soils are taken from experimental measurements (Knill, 1996) and previous numerical studies (Liu et al., 2020), in which the suction-dependent parameters are calibrated to match the runout distance observed in the field. The SWCC parameters are selected to best fit the experiment data from Gan and Fredlund (1995) using Van-Genuchten model, as shown in Fig. 12(a). To make the simulation time and computational cost practical for the explicit SPH scheme, an accelerated seepage analysis is conducted using an increased K_{sat} value (Yerro et al., 2015; Bandara et al., 2016). In present analysis, a value of 1.0×10^{-3} m/s is assigned to K_{sat} for the upper layers, following the study of Liu et al. (2020), to accelerate the seepage analysis. Fig. 12(b) shows the hydraulic conductivity curve of unsaturated soils used in the simulation at different matric suctions. The initial matric suction is taken as 50 kPa according to the numerical analysis on the same case by Cuomo et al. (2021). The ponding condition is assumed at the free surface with prescribed zero pore-water pressure for simulating the extreme rainfall scenarios (e.g., Wang et al., 2018; Lei et al., 2020; Feng et al., 2022). The initial node distribution is set as dp = 0.1 m, resulting in total 32,989 particles.

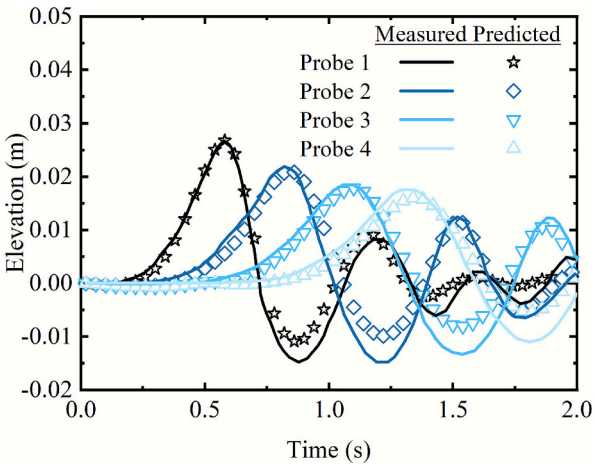

Fig. 17. Comparison of the free water surface profiles over time between SPH prediction and experiment measurements.

Fig. 13 shows the evolution of pore water pressure and equivalent deviatoric plastic strain. In the field observations, the landslide occurred in two phases: an initial minor failure involving tens of cubic meters of soil, followed by a major failure approximately 20 min later (Knill, 1996). This is consistent with the numerical simulation results, in which a local minor failure initiates at $t = 340$ s, and the major failure subsequently occurs at $t = 1860$ s. The developed model successfully reproduces the progressive failure pattern of the rainfall-induced landslide. Additionally, the wetting process due to infiltration and the propagation of the wetting front are well captured, with a smooth prediction of pore water pressure.

The deposition profile obtained from the SPH simulation is presented in Fig. 14, along with comparisons to field observations and results from other numerical studies, including a single-phase SPH model (Pastor et al., 2014) and a two-phase MPM (Liu et al., 2020). The simulation results by the proposed multiphase SPH model demonstrate reasonable agreement with both field observations and previous numerical studies.

4.4. Landslide-induced tsunami

This case refers to the simulation of landslide-induced tsunami to validate the soil-water interaction by the proposed multiphase model. The geometry and configuration of the numerical model are set to match the experiment conducted by Viroulet et al. (2013), as shown in Fig. 15. Initially, a granular mass with a 0.11 m × 0.11 m triangular cross-section is positioned on a 45° slope, supported by a vertical gate. Upon release, the granular materials enter the water and generate waves that subsequently propagate over time. At distances of 0.45 m, 0.75 m, 1.05 m, and 1.35 m from the gate, four water elevation gauges are located.

The material properties of the granular material are referenced from

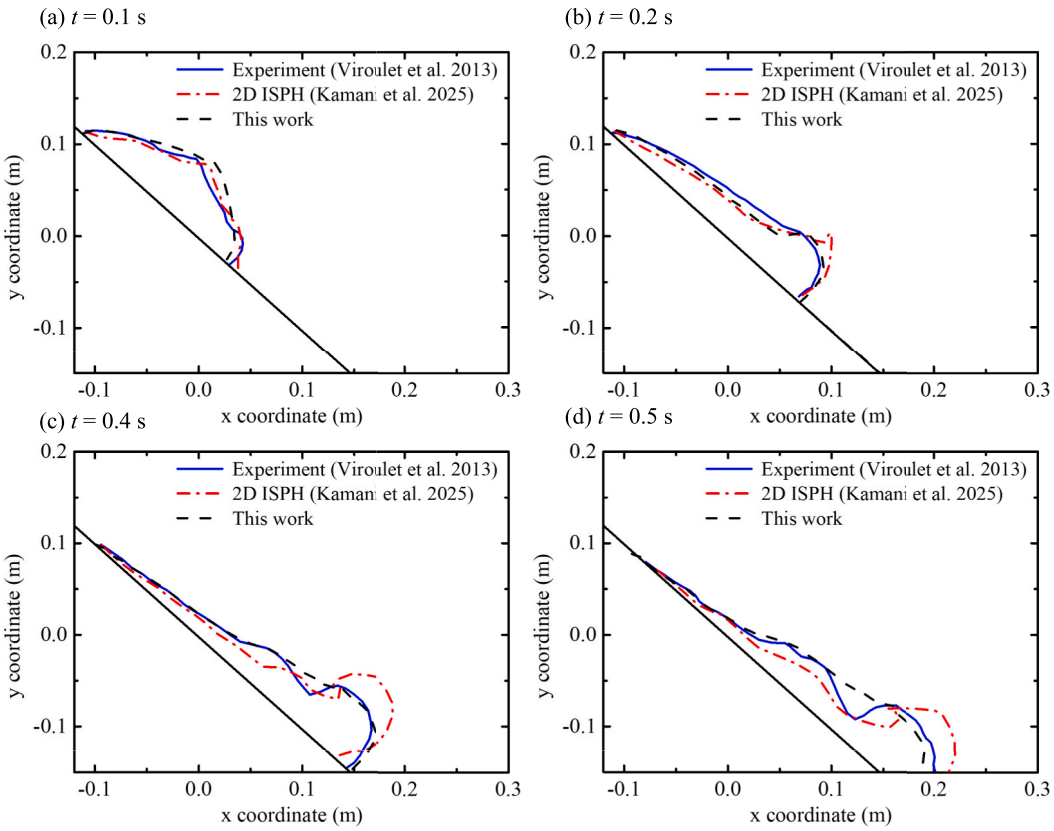

Fig. 18. Comparison of the landslide profiles between the numerical results and the experiment data (Viroulet et al., 2013).

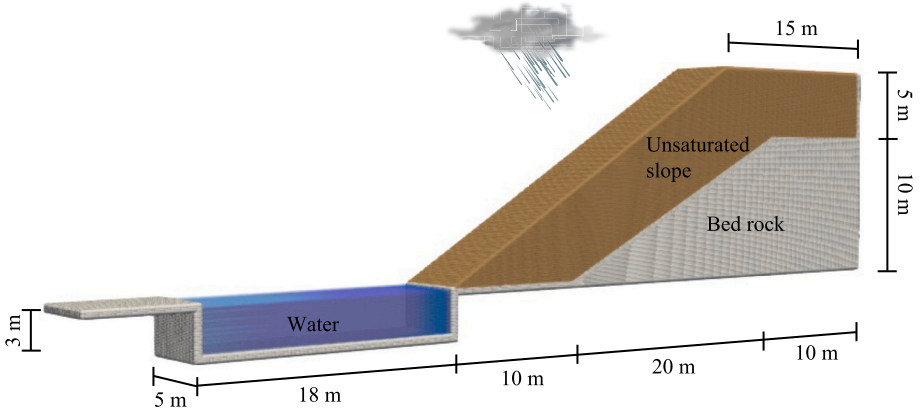

Fig. 19. Rainfall-landslide-tsunami event: geometries and numerical configuration.

Kamani et al. (2025), taking value of $E = 2$ MPa, $\nu = 0.3$, $\varphi = 22°$, $c = 0$ kPa, $\eta = 0$, and total density $\rho = 2500$ kg/m^3. Since no matric suction is involved in the simulation (i.e., $p_w = 0$), suction-related terms, including suction-dependent strength and the hydraulic constitutive relations, are not considered. The initial particle resolution is taken as dp = 0.004 m, resulting in total 1,460,801 particles.

Fig. 16 shows landslide-water impact process at different time instants. At the $t = 0.1$ s, the sliding material begins to impact the water surface, resulting in a localized increase in water pressure at the point of contact and the formation of an initial surface depression. As the simulation progresses to $t = 0.2$ s, the sliding mass penetrates further, displacing more water and producing a pronounced wave crest that propagates outward from the impact site. By $t = 0.5$ s, the granular material becomes submerged and dispersing, while the generated wave travels further across the water surface, with the pressure field clearly indicating a moving high-pressure front. Throughout the sequence, the simulation captures the complex interplay between the sliding mass flow and the water, with a noise-free pressure prediction.

Fig. 17 presents a quantitative comparison of free-surface wave elevation over time between numerical predictions and experimental measurements (Viroulet et al., 2013) at four gauges. At Probe 1 (closest to the impact location), both the measured and predicted profiles show a sharp initial peak, with good agreement in timing and amplitude. As the wave moves to Probes 2, 3, and 4, the peaks arrive later, and the amplitudes decrease. The predicted profiles generally match the main features of the measured waves, though a slight underestimation in amplitude can be observed on the downward side. This observation has also been reported in previous studies of the same case, such as the finite volume method (FVM) study by Rauter et al. (2022) and the SPH analysis by Mao and Guan (2023). Overall, the predictions accurately

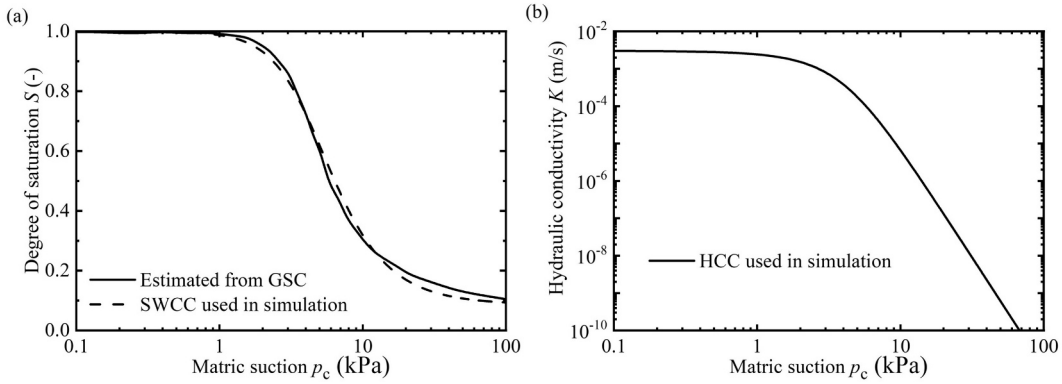

Fig. 20. Plot of the hydraulic model used in simulation: (a) SWCC and (b) HCC.

Table 3
Adopted material properties for the rainfall-landslide-tsunami simulation.

Paramters	Unit	Value
Soil grain density ρ_{s0}	kg/m^3	2690
Water density ρ_{w0}	kg/m^3	1000
Porosity ϕ	–	0.3
Water bulk modulus K_w	Pa	2×10^6
Saturated hydraulic conductivity K_{sat}	m/s	3×10^{-3}
Maximum degree of saturation S_{max}	–	1.0
Residual degree of saturation S_{min}	–	0.087
SWCC constant λ	–	0.61
SWCC constant p_{ref}	Pa	4350
Young's modulus E	MPa	6
Poisson's ratio ν	–	0.3
Peak cohesion c_p	kPa	6
Residual cohesion c_r	kPa	1
Peak friction angle φ_p	°	34
Residual friction angle φ_r	°	18
Strain-softening coefficient η	–	4
Suction-hardening coefficient A_s	°	0
Suction-hardening coefficient B_s	–	30
Suction-dependent cohesion c_{s0}	kPa	2

reproduce the propagation and attenuation of the wave as it travels away from the impact, demonstrating that the simulation effectively captures the essential dynamics of the landslide-generated wave and its propagation.

The evolution of landslide profile obtained from simulation at 4 different time instants is plotted in Fig. 18 against the experiment results and the numerical results using incompressible SPH (ISPH) by Kamani et al. (2025). As time progresses, the landslide front advances and deforms, with the simulations accurately capturing the stretching and sliding observed in the experiments. Both the results from the developed multiphase SPH model and the multiphase ISPH approach by Kamani et al. (2025) align well with the measured profiles, effectively reproducing the overall shape and position of the landslide.

5. Simulation of rainfall-landslide-tsunami cascades

The developed multiphase SPH model is finally applied to simulate the cascading multi-geohazards event of rainfall-landslide-tsunami. This case study aims to assess the applicability of the developed numerical method for predicting cascading disasters from the triggering of a landslide to its post-failure sliding processes and subsequent generation of tsunami.

Fig. 19 illustrates the geometry and configuration of the numerical model. An initially unsaturated soil slope, prone to failure under heavy rainfall, rests on the bedrock. Adjacent to the slope is a channel of water body, representing a river or reservoir environment that may be impacted by landslide-induced tsunamis. The soil properties used in the simulation are assumed to be those of Sakuragawa River sand, as utilized in the rainfall-induced landslide experiments conducted by Moriwaki et al. (2004) with experimental data available.

The SWCC model parameters, adopted from Yang et al. (2021), are based on estimations derived from the physical properties of Sakuragawa River sand. The original saturated hydraulic conductivity $K_{sat} = 3.0 \times 10^{-4}$ m/s is increased by one order of magnitude to $K_{sat} = 3.0 \times 10^{-3}$ m/s for an accelerated seepage analysis. Fig. 20 shows the plot of the hydraulic model used in simulation. The strength parameters are taken from Feng et al. (2024a), based on the reported measurements by Moriwaki et al. (2004) and simulations of the physical experiment, with the inclusion of cohesion in this study. Table 3 lists the adopted material properties in the simulation.

The analysis presumes an initial unsaturated condition for the slope with a constant matric suction of 7.0 kPa, corresponding to an initial degree of saturation, $S_{w0} = 0.46$. A specified vertical discharge with intensity of i is prescribed to the slope surface for initiating the water infiltration. To simulate the heavy rainfall, the ratio of $i/K_{sat} = 1.0$ is applied in the simulation (Rahardjo et al., 2007). The initial particle resolutions are set to dp = 0.1 m, resulting in total 1,436,550 particles.

Fig. 21 shows the simulated evolution of cascading rainfall-landslide-tsunami event. Initially, the unsaturated soil slope remains stable on the bedrock, with the adjacent water body undisturbed. As rainfall continues, the slope progressively becomes saturated from the free surface downward, resulting in the propagation of a saturated wetting front. Failure initiates at $t = 218$ s from the slope surface. This observed shallow landslide is consistent with other numerical reports (Ran et al., 2018; Lee et al., 2021) as well as field experiment (Guo et al., 2020; Sun et al., 2021) under heavy rainfall. After the onset of failure, a sliding mass is mobilised and rapidly moves downslope, impacting the water body at $t = 225$ s. This interaction generates a high-velocity wave, producing complex flow patterns and a propagating surge. In addition, the prescribed rainfall infiltration is accurately applied at the free surface using the adopted free-surface boundary treatment, resulting in a clear increase of pore water pressure from the surface. As the wetting front advances, the slope toe becomes fully saturated at $t = 219$ s, where the specified flux boundary is switched to a zero-pressure boundary to represent ponding conditions. Following the landslide's initiation, the impact of the sliding mass on the water body causes a local rise in water pressure. These results demonstrate that the proposed multiphase SPH model effectively captures the essential physical evolution during the cascading process, with a smooth and nearly noise-free prediction of both pore water pressure and free-surface water pressure.

Fig. 22 shows the calculated results of the landslide dynamics during the post-failure process, characterised by the equivalent deviatoric plastic strain and motion velocity. The rainfall-induced landslide initiates at $t = 218$ s, where the accumulation of plastic strain forms a major sliding surface, triggering a localized, low-velocity movement. By $t = 220$ s, driven by continued rainfall and strain-softening of sliding mass,

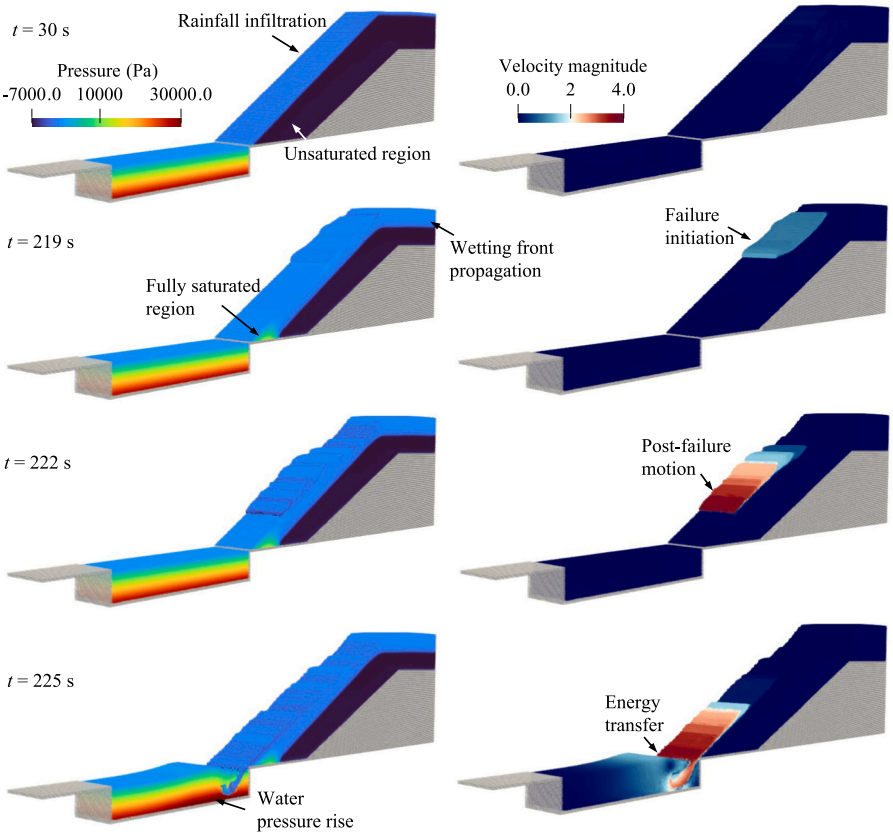

Fig. 21. Cascading process in the multi-geohazards evolution: from rainfall infiltration to landslide initiation and landslide-induced tsunami-like wave.

this initial sliding block accelerates downslope and results in a secondary failure surface, marking the onset of the retrogressive failure mechanism. This backward propagation of instability becomes more pronounced at $t = 222$ s, developing into a distinct horst-and-graben structure composed of raised (horst) and down-dropped (graben) blocks. During this stage, the leading edge of the slide exhibits high-velocity motion. Finally, at $t = 223$ s, the failure zone has visibly enlarged as the sliding system propagates further upslope. In essence, the simulated sequence clearly reproduces the retrogressive failure pattern of landslide due to rainfall, progressively increasing the total volume of landslide and creating its characteristic stepped topography.

Beyond the retrogressive failure, the simulation captures the dynamics along the landslide path. As the mass travels, basal entrainment occurs at the flow front, while mass deposition is observed behind it, leading to a bulking of the sliding zone as illustrated in Fig. 23. This combined entrainment-deposition dynamic is consistent with field observations of rainfall-induced debris flows (Dietrich and Krautblatter, 2019; Su et al., 2024). These observations highlight the necessity for a unified numerical framework capable of accurately predicting the full evolution of landslide volume and velocity.

Fig. 24 provides a detailed view of the landslide-tsunami dynamics following the impact. The sequence begins at $t = 224$ s as the sliding mass impacts the water body, displacing water and transferring momentum to initiate wave generation. Just one second later, at $t = 225$ s, the impact has formed a distinct first wave that propagates outward, leaving a low-flow zone near the landslide toe. This low-flow zone, also observed in experimental and other numerical studies for landslide-tsunamis (Viroulet et al., 2013; Kamani et al., 2025; Yi et al., 2025), may be attributed to a circulatory motion that draws water in behind the moving landslide. By $t = 226$ s, the first wave continues across the water channel while the ongoing sliding process generates a second wave. The event escalates at $t = 227$ s when the initial wave reaches the left bank of the water body, causing significant overtopping, while the second wave begins to break closer to the source. Finally, at $t = 229$ s, the simulation shows the consequences of wave impact, with flooding and sweeping occurring on the adjacent ground. In the water channel, the complex interaction between the underwater landslide and the circulatory motion of water creates a large, distinct vortex. Overall, the proposed method effectively captures the key physical phenomena of the landslide-tsunami transition, from initial impact and wave propagation to the final consequences. Furthermore, the proposed method also provides the fine details of hydrodynamic during the process such as wave breaking, circulation, and vortex formation.

To summarise, these results indicate that the proposed multiphase SPH model can effectively capture the entire process of cascading multi-hazards, from pore water flow induced by rainfall, landslide initiation due to saturation, to the post-failure evolution of the sliding mass and subsequent dynamics of landslide-generated tsunami as well as final impacts including overtopping and flooding. In comparison with existing methods such as LS-RAPID and LS-TSUNAMI, this new method provides a quantitative, deterministic analysis of hazard initiation (for example location and landslide volume) and subsequent evolution under a given infiltration flux, allowing for a physics-based simulation of multi-hazard cascades with less empiricism and uncertainty. Such a holistic simulation framework can capture the evolution of pore water pressure and effective stress within the soil mass as well as the hydrodynamics of the water body during the whole disaster process and the two-way coupled interaction between the landslide and the external water body. This modelling capacity can provide a deeper understanding of the landslide mechanism and insights into the dynamics of landslide-tsunami cascades. It also provides predictions of the scale and deposition morphology of the sliding mass in the water, which is critical for assessing the potential formation of barrier lakes by the landslide deposit.

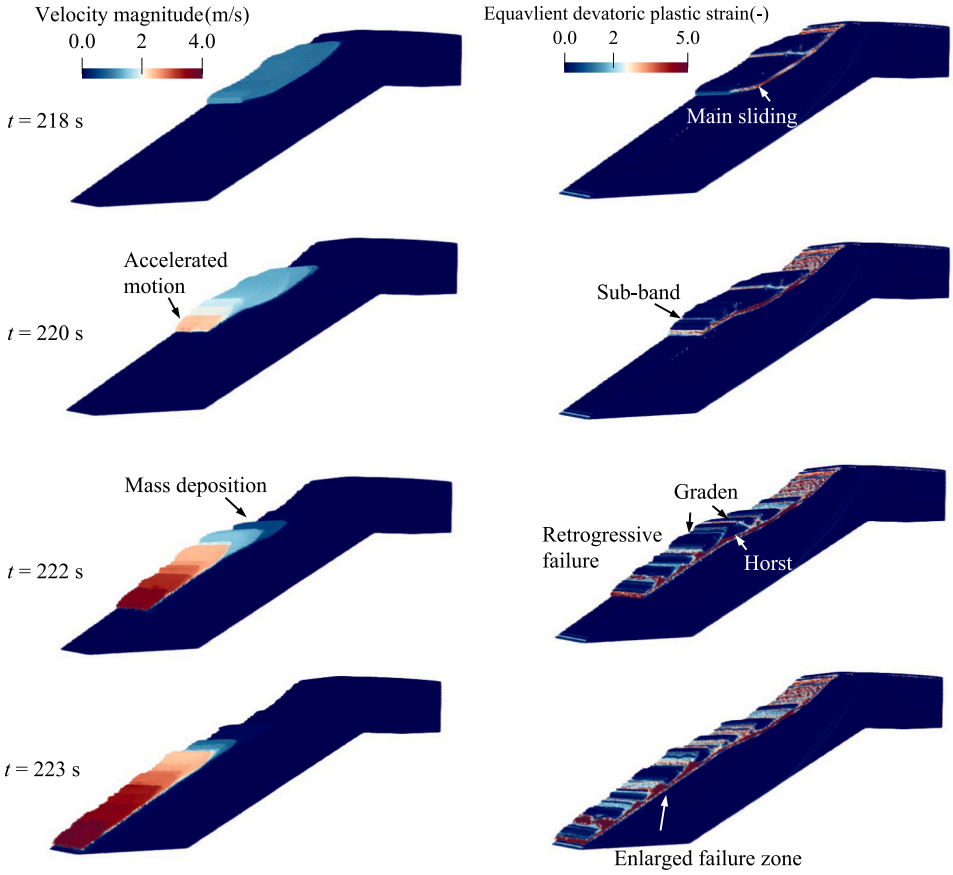

Fig. 22. Time evolution of sliding mass motion and failure surface development during the post-failure process of rainfall-induced landslides.

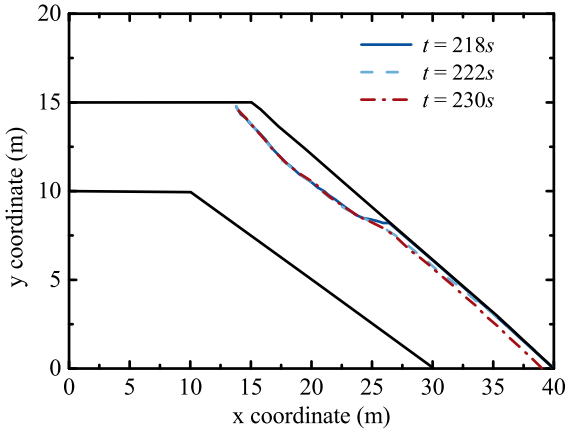

Fig. 23. Bulking of the sliding zone during the landslide mass movement.

The proposed method is also suited for real-world applications. Its meshfree SPH framework provides geometric flexibility to handle complex topography, allowing real terrain data, such as digital elevation models, to be directly converted into a numerical model. Furthermore, the GPU-accelerated implementation enables the practical simulation of large-scale, three-dimensional problems involving tens of millions of particles (Feng et al., 2025b). A primary limitation, however, is the small time step imposed by the CFL condition due to the use of explicit time integration scheme. In this study and other studies using explicit scheme (e.g., Yerro et al., 2015; Bandara et al., 2016; Liu et al., 2020), this is mitigated by an accelerated seepage analysis with increased permeability. To allow the use of a larger time step and the simulation of realistic time scales (e.g., over weeks or months), the development of implicit, semi-implicit, or adaptive time integration schemes will be necessary and will be the future direction.

6. Conclusions

This paper presents a novel 3D multiphase SPH framework for modelling coupled soil-water interactions, to address the formidable challenge of simulating multi-hazard cascades such as rainfall-induced landslides-tsunamis events. The key advancement of this work lies in its fully unified approach, which integrates the hydro-mechanical processes triggering slope failure with the subsequent large-deformation dynamics and fluid interaction. The primary contributions of this study include:

a) Unified multiphase formulation: The proposed multiphase SPH model incorporates the *u–w–p* formulation of Biot's theory for unsaturated/saturated soils, enabling the simulation of coupled pore flow and soil deformation under different saturation condition, as well as the dynamic interaction between soil and external water. This constitutes a significant enhancement over existing multiphase SPH models for soil-water interaction.
b) Robust numerical schemes: The introduction of a numerical density concept mitigates interfacial instability issues, while the extension of the δ-SPH scheme ensures a smooth and stable pressure field for both pore water and external water.
c) Advanced boundary treatments: The 3D implementation of hydraulic and solid boundary conditions allows for the quantitative and realistic simulation of triggering mechanisms, such as rainfall infiltration.

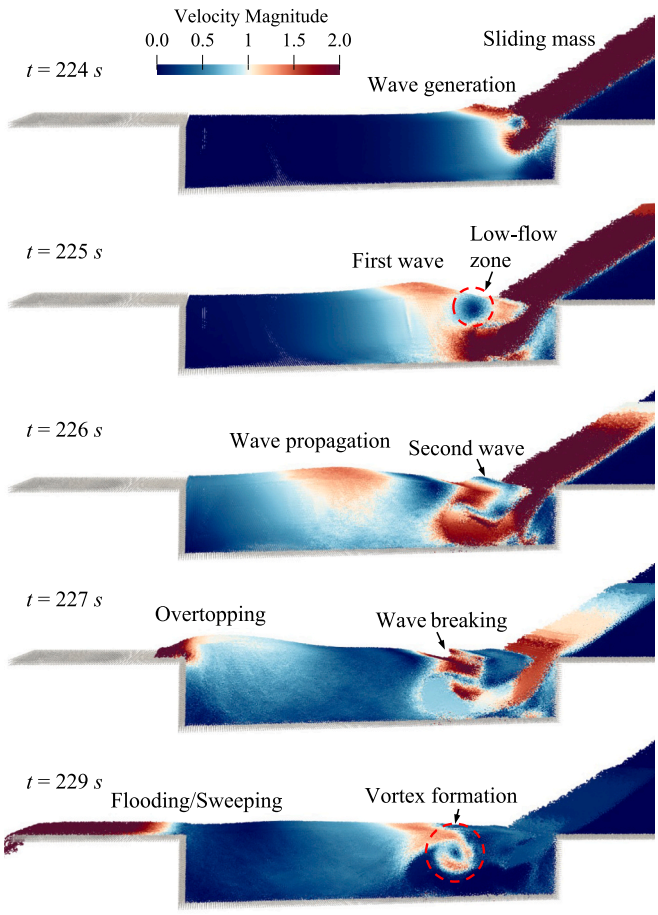

Fig. 24. Cascading consequences of rainfall-landslide-tsunami: wave generation, propagation, and subsequent overtopping/flooding.

d) High-performance computing: Implementation within a CUDA-enabled, GPU-accelerated solver makes large-scale 3D simulations of complex geophysical events computationally feasible.

The proposed framework was rigorously validated against a series of reference solutions and benchmark experiments, demonstrating excellent agreement in simulating pore water flow in saturated/unsaturated soils, coupled flow-deformation, landslide runout, and tsunami generation. Its capability was further proven through a full 3D simulation of a cascading rainfall-landslide-tsunami event, capturing the entire process from initiation to impact. To the best of our knowledge, this represents the first unified computational framework capable of modelling such complex, coupled multi-physics evolutions within a single, consistent numerical environment. This work not only provides a powerful tool for the predictive analysis of geophysical hazards but also establishes a new foundation for future research. The model can be extended to investigate a broader range of triggering mechanisms and their interplay in multi-hazard chains, including earthquakes, reservoir level fluctuations, and glacier retreat, ultimately contributing to more effective physics-based risk assessment and mitigation strategies.

CRediT authorship contribution statement

Ruofeng Feng: Writing – original draft, Visualization, Validation, Software, Methodology, Investigation, Data curation, Conceptualization. **Jidong Zhao:** Writing – review & editing, Supervision, Resources, Project administration, Funding acquisition, Conceptualization. **Jianyu Chen:** Writing – review & editing, Validation, Methodology, Data curation.

Declaration of competing interest

The authors declare that they have no known competing financial interests or personal relationships that could have appeared to influence the work reported in this paper.

Acknowledgements

This work was financially supported by the National Natural Science Foundation of China (Key Project #52439001), and the Research Grants Council of Hong Kong (GRF 16203123, 16208224, 16217225, CRF C7085-24G, RIF R6008-24, TRS T22-607/24 N, and T22-606/23-R).

Data availability

Data will be made available on request.

References

Altomare, C., Crespo, A.J., Domínguez, J.M., Gomez-Gesteira, M., Suzuki, T., Verwaest, T., 2015. Applicability of Smoothed Particle Hydrodynamics for estimation of sea wave impact on coastal structures. Coast. Eng. 96, 1–12.
Antuono, M., Colagrossi, A., Marrone, S., 2012. Numerical diffusive terms in weakly-compressible SPH schemes. Comput. Phys. Commun. 183 (12), 2570–2580.
Aránguiz, R., Caamaño, D., Espinoza, M., Gómez, M., Maldonado, F., Sepúlveda, V., Rogel, I., Oyarzun, J.C., Duhart, P., 2023. Analysis of the cascading rainfall–landslide–tsunami event of June 29th, 2022, Todos los Santos Lake, Chile. Landslides 20 (4), 801–811.
Asai, M., Fujioka, S., Saeki, Y., Morikawa, D.S., Tsuji, K., 2023. A class of second-derivatives in the Smoothed Particle Hydrodynamics with 2nd-order accuracy and its application to incompressible flow simulations. Comput. Methods Appl. Mech. Eng. 415, 116203.
Bandara, S., Ferrari, A., Laloui, L., 2016. Modelling landslides in unsaturated slopes subjected to rainfall infiltration using material point method. Int. J. Numer. Anal. Methods Geomech. 40 (9), 1358–1380.
Bui, H.H., Nguyen, G.D., 2021. Smoothed particle hydrodynamics (SPH) and its applications in geomechanics: from solid fracture to granular behaviour and multiphase flows in porous media. Comput. Geotech. 138, 104315.
Chen, J.Y., Lien, F.S., Peng, C., Yee, E., 2020. GPU-accelerated smoothed particle hydrodynamics modeling of granular flow. Powder Technol. 359, 94–106.
Chen, J.Y., Feng, D.L., Lien, F.S., Yee, E., Deng, S.X., Gao, F., Peng, C., 2021. Numerical modelling of interaction between aluminium structure and explosion in soil. Appl. Math. Model. 99, 760–784.
Cheng, Z., Zhao, S., Chen, H., Zhao, J., 2026. Stabilized explicit material point method for fluid flow and fluid-structure interaction simulations using dual high-order B-spline volume averaging. Comput. Methods Appl. Mech. Eng. 448, 118428.
Cuomo, S., Di Perna, A., Martinelli, M., 2021. Modelling the spatio-temporal evolution of a rainfall-induced retrogressive landslide in an unsaturated slope. Eng. Geol. 294, 106371.
Dai, Z., Huang, Y., Cheng, H., Xu, Q., 2017. SPH model for fluid–structure interaction and its application to debris flow impact estimation. Landslides 14 (3), 917–928.
Dai, Z., Xie, J., Jiang, M., 2023a. A coupled peridynamics–smoothed particle hydrodynamics model for fracture analysis of fluid–structure interactions. Ocean Eng. 279, 114582.
Dai, Z., Li, X., Lan, B., 2023b. Three-dimensional modeling of tsunami waves triggered by submarine landslides based on the smoothed particle hydrodynamics method. J. Mar. Sci. Eng. 11 (10), 2015.
Dai, Z., Hu, C., Song, K., 2025. Multiphase flow model for surge waves generated by flow-like landslide based on smoothed particle hydrodynamics. Phys. Fluids 37 (8).
Dietrich, A., Krautblatter, M., 2019. Deciphering controls for debris-flow erosion derived from a LiDAR-recorded extreme event and a calibrated numerical model (Roßbichelbach, Germany). Earth Surf. Process. Landf. 44 (6), 1346–1361.
Domínguez, J.M., Fourtakas, G., Altomare, C., Canelas, R.B., Tafuni, A., García-Feal, O., Martínez-Estévez, I., Mokos, A., Vacondio, R., Crespo, A.J., Rogers, B.D., 2022. DualSPHysics: from fluid dynamics to multiphysics problems. Comput. Part. Mech. 9 (5), 867–895.
Duc, D.M., Khang, D.Q., Duc, D.M., Ngoc, D.M., Quynh, D.T., Thuy, D.T., Giang, N.K.H., Van Tien, P., Ha, N.H., 2020. Analysis and modeling of a landslide-induced tsunami-like wave across the Truong river in Quang Nam province, Vietnam. Landslides 17 (10), 2329–2341.
Feng, R., Fourtakas, G., Rogers, B.D., Lombardi, D., 2021. Large deformation analysis of granular materials with stabilized and noise-free stress treatment in smoothed particle hydrodynamics (SPH). Comput. Geotech. 138, 104356.
Feng, R., Fourtakas, G., Rogers, B.D., Lombardi, D., 2022. Two-phase fully-coupled smoothed particle hydrodynamics (SPH) model for unsaturated soils and its application to rainfall-induced slope collapse. Comput. Geotech. 151, 104964.
Feng, R., Fourtakas, G., Rogers, B.D., Lombardi, D., 2024a. A general smoothed particle hydrodynamics (SPH) formulation for coupled liquid flow and solid deformation in porous media. Comput. Methods Appl. Mech. Eng. 419, 116581.

Feng, R., Fourtakas, G., Rogers, B.D., Lombardi, D., 2024b. Modelling internal erosion using 2D smoothed particle hydrodynamics (SPH). J. Hydrol. 639, 131558.
Feng, D., Gan, L., Xiong, M., Li, W., Huang, Y., 2025a. Uncertainty analysis of 3D post-failure behavior in landslide and reinforced slope based on the SPH method and the random field theory. Eng. Geol. 350, 108017.
Feng, R., Zhao, J., Fourtakas, G., Rogers, B.D., 2025b. GeoDualSPHysics: A High-Performance SPH Solver for Large Deformation Modelling of Geomaterials with Two-Way Coupling to Multi-Body Systems. Under Review, p. 109965. https://doi.org/10.1016/j.cpc.2025.109965.
Gan, J.K.M., Fredlund, D.G., 1995. Direct Shear Testing of a Hong Kong Soil under Various Applied Matric Suctions. GEO Report No. 11.. Geotechnical Engineering Office, Hong Kong.
Gardner, W.R., 1958. Some steady-state solutions of the unsaturated moisture flow equation with application to evaporation from a water table. Soil Sci. 85 (4), 228–232.
Grenier, N., Antuono, M., Colagrossi, A., Le Touzé, D., Alessandrini, B., 2009. An Hamiltonian interface SPH formulation for multi-fluid and free surface flows. J. Comput. Phys. 228 (22), 8380–8393.
Guo, W., Xu, X., Wang, W., Zhu, T., Liu, Y., 2020. Experimental study of shallow mass movements on gully slopes and associated sediment under rainfall on the Chinese loess plateau. Geomorphology 350, 106919.
Hammani, I., Marrone, S., Colagrossi, A., Oger, G., Le Touzé, D., 2020. Detailed study on the extension of the δ-SPH model to multi-phase flow. Comput. Methods Appl. Mech. Eng. 368, 113189.
Hoang, T.N., Bui, H.H., Nguyen, T.T., Nguyen, T.V., Nguyen, G.D., 2024. Development of free-field and compliant base SPH boundary conditions for large deformation seismic response analysis of geomechanics problems. Comput. Methods Appl. Mech. Eng. 432, 117370.
Iverson, R.M., 2000. Landslide triggering by rain infiltration. Water Resour. Res. 36 (7), 1897–1910.
Ju, L.Y., Xiao, T., He, J., Xu, W.F., Xiao, S.H., Zhang, L.M., 2025. A simulation-enabled slope digital twin for real-time assessment of rain-induced landslides. Eng. Geol. 353, 108116.
Kamani, N., Zeraatgar, H., Ketabdari, M.J., 2025. Numerical simulation of fluid-granular interactions (FGI) using improved two-phase incompressible smooth particle hydrodynamics. Ocean Eng. 324, 120662.
Khayyer, A., Gotoh, H., Shimizu, Y., Gotoh, K., Falahaty, H., Shao, S., 2018. Development of a projection-based SPH method for numerical wave flume with porous media of variable porosity. Coast. Eng. 140, 1–22.
Knill, J., 1996. Report on the Fei Tsui Road landslide of 13 August 1995. GEO Report no. 188. Geotechnical Engineering Office, Hong Kong.
Lee, W.L., Martinelli, M., Shieh, C.L., 2021. An investigation of rainfall-induced landslides from the pre-failure stage to the post-failure stage using the material point method. Front. Earth Sci. 9, 764393.
Lei, X., He, S., Chen, X., Wong, H., Wu, L., Liu, E., 2020. A generalized interpolation material point method for modelling coupled seepage-erosion-deformation process within unsaturated soils. Adv. Water Resour. 141, 103578.
Liakopoulos, A.C., 1964. Transient Flow through Unsaturated Porous Media. University of California, Berkeley.
Lian, Y., Bui, H.H., Nguyen, G.D., Haque, A., 2023. An effective and stabilised (u− pl) SPH framework for large deformation and failure analysis of saturated porous media. Comput. Methods Appl. Mech. Eng. 408, 115967.
Lian, Y., Bui, H.H., Nguyen, G.D., Zhao, S., Haque, A., 2024. A computationally efficient SPH framework for unsaturated soils and its application to predicting the entire rainfall-induced slope failure process. Géotechnique 74 (8), 787–805.
Liu, M.B., Liu, G.R., 2006. Restoring particle consistency in smoothed particle hydrodynamics. Appl. Numer. Math. 56 (1), 19–36.
Liu, X., Wang, Y., Li, D.Q., 2020. Numerical simulation of the 1995 rainfall-induced Fei Tsui Road landslide in Hong Kong: new insights from hydro-mechanically coupled material point method. Landslides 17 (12), 2755–2775.
Ma, Y., Asai, M., Han, Z., Chen, G., 2024. Two-layer multi-state SPH modelling of momentum growth and its feedback in viscous debris flow on wet bed sediment. Eng. Geol. 343, 107804.
Mao, Y., Guan, M., 2023. Mesh-free simulation of height and energy transfer of landslide-induced tsunami waves. Ocean Eng. 284, 115219.
Marrone, S., Antuono, M.A.G.D., Colagrossi, A., Colicchio, G., Le Touzé, D., Graziani, G., 2011. δ-SPH model for simulating violent impact flows. Comput. Methods Appl. Mech. Eng. 200 (13–16), 1526–1542.
Meng, Z.F., Wang, P.P., Zhang, A.M., Ming, F.R., Sun, P.N., 2020. A multiphase SPH model based on Roe's approximate Riemann solver for hydraulic flows with complex interface. Comput. Methods Appl. Mech. Eng. 365, 112999.
Mokos, A., Rogers, B.D., Stansby, P.K., 2017. A multi-phase particle shifting algorithm for SPH simulations of violent hydrodynamics with a large number of particles. J. Hydraul. Res. 55 (2), 143–152.
Monaghan, J.J., 2005. Smoothed particle hydrodynamics. Rep. Prog. Phys. 68 (8), 1703.
Moriwaki, H., Inokuchi, T., Hattanji, T., Sassa, K., Ochiai, H., Wang, G., 2004. Failure processes in a full-scale landslide experiment using a rainfall simulator. Landslides 1 (4), 277–288.
Ng, C.W.W., Zhou, C., Chiu, C.F., 2020. Constitutive modelling of state-dependent behaviour of unsaturated soils: an overview. Acta Geotech. 15 (10), 2705–2725.
Nguyen, D.T., Bui, H.H., Lian, Y., Nguyen, T.T., Nguyen, G.D., Bouazza, A., 2025. A CASM-X constitutive model for unsaturated soils and its application to model wetting-induced slope collapse using SPH. Comput. Geotech. 186, 107353.
Paronuzzi, P., Bolla, A., 2012. The prehistoric Vajont rockslide: an updated geological model. Geomorphology 169, 165–191.
Pastor, M., Blanc, T., Haddad, B., Petrone, S., Sanchez Morles, M., Drempetic, V., Issler, D., Crosta, G.B., Cascini, L., Sorbino, G., Cuomo, S., 2014. Application of a SPH depth-integrated model to landslide run-out analysis. Landslides 11 (5), 793–812.
Rahardjo, H., Ong, T.H., Rezaur, R.B., Leong, E.C., 2007. Factors controlling instability of homogeneous soil slopes under rainfall. J. Geotech. Geoenviron. Eng. 133 (12), 1532–1543.
Ran, Q., Hong, Y., Li, W., Gao, J., 2018. A modelling study of rainfall-induced shallow landslide mechanisms under different rainfall characteristics. J. Hydrol. 563, 790–801.
Rauter, M., Viroulet, S., Gylfadóttir, S.S., Fellin, W., Løvholt, F., 2022. Granular porous landslide tsunami modelling–the 2014 Lake Askja flank collapse. Nat. Commun. 13 (1), 678.
Ren, Z., Li, D., Li, Z., Wang, H., Liu, J., Qu, Z., Li, Y., 2024. Spatial-temporal evolution mechanism of mass transfer under synergetic gaseous and vapour cavitating effects in a micropump. Energy 286, 129545.
Sassa, K., Dang, K., Yanagisawa, H., He, B., 2016. A new landslide-induced tsunami simulation model and its application to the 1792 Unzen-Mayuyama landslide-and-tsunami disaster. Landslides 13 (6), 1405–1419.
Schrefler, B.A., Scotta, R., 2001. A fully coupled dynamic model for two-phase fluid flow in deformable porous media. Comput. Methods Appl. Mech. Eng. 190 (24–25), 3223–3246.
Su, B., Li, Y., Han, Z., Ma, Y., Wang, W., Ruan, B., Guo, W., Xie, W., Tan, S., 2024. Topography-based and vectorized algorithm for extracting physical quantities in 3D-SPH form and its application in debris-flow entrainment modeling. Eng. Geol. 340, 107693.
Su, Z., Kang, X., Ding, X., Wang, S., Li, D., 2026. SPH–DEM modeling of rainfall-induced slope failure in partially saturated soil–rock mixture. Comput. Geotech. 189, 107635.
Sun, P.N., Colagrossi, A., Marrone, S., Zhang, A.M., 2017. The δplus-SPH model: simple procedures for a further improvement of the SPH scheme. Comput. Methods Appl. Mech. Eng. 315, 25–49.
Sun, P.N., Colagrossi, A., Marrone, S., Antuono, M., Zhang, A.M., 2019. A consistent approach to particle shifting in the δ-Plus-SPH model. Comput. Methods Appl. Mech. Eng. 348, 912–934.
Sun, P., Wang, H., Wang, G., Li, R., Zhang, Z., Huo, X., 2021. Field model experiments and numerical analysis of rainfall-induced shallow loess landslides. Eng. Geol. 295, 106411.
Torzoni, M., Tezzele, M., Mariani, S., Manzoni, A., Willcox, K.E., 2024. A digital twin framework for civil engineering structures. Comput. Methods Appl. Mech. Eng. 418, 116584.
Vega, J.A., Hidalgo, C.A., 2016. Quantitative risk assessment of landslides triggered by earthquakes and rainfall based on direct costs of urban buildings. Geomorphology 273, 217–235.
Violeau, D., Rogers, B.D., 2016. Smoothed particle hydrodynamics (SPH) for free-surface flows: past, present and future. J. Hydraul. Res. 54 (1), 1–26.
Viroulet, S., Sauret, A., Kimmoun, O., Kharif, C., 2013. Granular collapse into water: toward tsunami landslides. J. Vis. 16 (3), 189–191.
Wang, B., Vardon, P.J., Hicks, M.A., 2018. Rainfall-induced slope collapse with coupled material point method. Eng. Geol. 239, 1–12.
Wang, J., Xiao, L., Ward, S.N., Du, J., 2021. Tsunami Squares modeling of the 2007 Dayantang landslide generated waves considering the effects in slide/water interactions. Eng. Geol. 284, 106032.
Yang, K.H., Nguyen, T.S., Rahardjo, H., Lin, D.G., 2021. Deformation characteristics of unstable shallow slopes triggered by rainfall infiltration. Bull. Eng. Geol. Environ. 80 (1), 317–344.
Yang, C., Zhu, F., Zhao, J., 2024. Coupled total-and semi-Lagrangian peridynamics for modelling fluid-driven fracturing in solids. Comput. Methods Appl. Mech. Eng. 419, 116580.
Yang, C., Zhao, J., Zhu, F., Feng, R., 2025. A multi-horizon peridynamics for coupled fluid flow and heat transfer. J. Fluid Mech. 1010, A66.
Yerro, A., Alonso, E.E., Pinyol, N.M., 2015. The material point method for unsaturated soils. Géotechnique 65 (3), 201–217.
Yerro, A., Soga, K., Bray, J., 2019. Runout evaluation of Oso landslide with the material point method. Can. Geotech. J. 56 (9), 1304–1317.
Yi, C., Chen, J., Hu, M., Feng, D., 2025. A new SPH multi-phase interface treatment method for soil–water interaction modeling. Comput. Geotech. 185, 107282.
Yu, J., Zhao, J., Liang, W., Zhao, S., 2024. A semi-implicit material point method for coupled thermo-hydro-mechanical simulation of saturated porous media in large deformation. Comput. Methods Appl. Mech. Eng. 418, 116462.
Yu, J., Liang, W., Zhao, J., 2025. Enhancing dynamic modeling of porous media with compressible fluid: a THM material point method with improved fractional step formulation. Comput. Methods Appl. Mech. Eng. 444, 118100.
Zhang, C., Hu, X.Y., Adams, N.A., 2017. A weakly compressible SPH method based on a low-dissipation Riemann solver. J. Comput. Phys. 335, 605–620.

Zhang, R., Xiong, W., Ma, X., Cai, C.S., 2024a. Mesh-free SPH modelling of sediment scouring and flushing considering grains transport and transformation. Eng. Applicat. Computation. Fluid Mechan. 18 (1), 2367510.
Zhang, S., Zhang, C., Hu, X., Lourenço, S.D., 2024b. A Riemann-based SPH method for modelling large deformation of granular materials. Comput. Geotech. 167, 106052.
Zhang, S., Wu, D., Lourenço, S.D., Hu, X., 2025. A generalized non-hourglass updated Lagrangian formulation for SPH solid dynamics. Comput. Methods Appl. Mech. Eng. 440, 117948.
Zhou, X., Lu, D., Zhang, Y., Du, X., Rabczuk, T., 2022. An open-source unconstrained stress updating algorithm for the modified Cam-clay model. Comput. Methods Appl. Mech. Eng. 390, 114356.
Zhou, M., Shi, Z., Peng, C., Peng, M., Cui, K.F.E., Li, B., Zhang, L., Zhou, G.G., 2024. Two-phase modelling of erosion and deposition process during overtopping failure of landslide dams using GPU-accelerated ED-SPH. Comput. Geotech. 166, 105944.
Zubeldia, E.H., Fourtakas, G., Rogers, B.D., Farias, M.M., 2018. Multi-phase SPH model for simulation of erosion and scouring by means of the shields and Drucker–Prager criteria. Adv. Water Resour. 117, 98–114.
Zhou, X., Lu, D.C., Zhao, J.D., Zhang, Y.N., Gao, Z.W., Rabczuk, T., Du, X.L., 2025. Material characteristic length insensitive nonlocal modelling: A computationally efficient scaled nonlocal integral method. Comput. Geotech. 188, 107587.